



Bi-functional CeO₂ coated NiCo-MgAl core-shell catalyst with high activity and resistance to coke and H₂S poisoning in methane dry reforming

Sonali Das^{a,1}, Kang Hui Lim^{a,1}, Terry Z.H. Gani^a, Saeed Aksari^a, Sibudjing Kawi^{a,*}

^a Department of Chemical and Biomolecular Engineering, National University of Singapore, Singapore 119260, Singapore

ARTICLE INFO

Keywords:

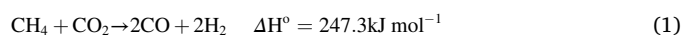
Dry reforming of methane
Core shell catalyst
Coke resistance
H₂S tolerance
Hydrogen production

ABSTRACT

A bi-functional core-shell catalyst is reported for CO₂ reforming of methane, that combines high catalytic activity with resistance to both coke formation and deactivation by H₂S poisoning. We developed a NiCo-MgAl@CeO₂ core-shell catalyst incorporating a layered double hydroxide-derived core and a CeO₂ shell that shows high DRM activity and stability and enhanced resistance to H₂S-induced deactivation, while maintaining negligible coke formation through the steric confinement effect of the core-shell morphology and the participation of lattice oxygen of CeO₂ in coke oxidation. Co addition in the core delays the onset of catalyst deactivation in the presence of H₂S by altering sulfur chemisorption kinetics, and the lattice oxygen of the CeO₂ shell suppresses steady-state catalyst deactivation under continuous H₂S flow by oxidatively removing H₂S under continuous replenishment by CO₂. The synergistic and complementary properties of the NiCo-containing core and CeO₂ shell results in simultaneous coke resistance and H₂S tolerance of the bi-functional catalyst.

1. Introduction

Dry reforming of methane or biogas with CO₂ (Eq. (1)) is gaining increasing research attention worldwide because it is a route to convert two major greenhouse gases into syngas, which can be used as fuel, as a source of hydrogen, or for producing valuable chemicals through methanol or Fischer Tropsch synthesis. Dry reforming of alternate renewable methane sources such as biogas, which naturally contain CO₂ in significant proportions, is an attractive way of upgrading them into a hydrogen-rich reformat mixture with higher calorific value.



The primary challenge for the large-scale implementation of dry reforming is the rapid formation of coke on the catalyst, which can lead to the blocking of active sites or pressure build-up inside the reactor by catalyst bed expansion [1,2]. Sintering and agglomeration of metal nanoparticles in the catalyst under harsh reaction conditions is another closely related cause of catalyst deactivation. In the last decade, there has been intense research aimed at improving the coke and sintering resistance of DRM catalysts, and several strategies have been proposed to that effect, such as decreasing metal particle size [3,4], alloying with other metals [5,6], increasing metal support interaction [7,8], confining

metal particles in core-shell morphologies [9], etc.

However, although coke inhibition and resistance to metal sintering remain the primary and most important catalyst requirements for long term operation of DRM, another major challenge for DRM is the effect of sulfur-containing compounds on the catalytic activity. The poisoning of catalysts by sulfur compounds is especially a problem for renewable sources of methane such as biogas. Apart from the major components of CH₄ and CO₂, biogas also contains trace amounts of impurities like H₂S, ammonia and siloxanes [10]. H₂S in biogas (0 – 200 ppm) may lead to catalyst poisoning, as well as equipment corrosion [10]. Several studies have reported that the catalyst activity could be significantly affected by very low H₂S concentration (even a few ppm) [11–13]. H₂S is also present in sour natural gas. Poisoning by H₂S also poses a concern in solid oxide fuel cells for the utilization of natural gas, biogas, or biomass gasifier syngas [14,15]. Sour sources of methane containing H₂S are subjected to sweetening processes to remove the sulfur compounds to acceptable concentrations before being fed to reforming reactors. However, it is important for the reforming catalysts to possess some resistance to sulfur poisoning in order to be able to accommodate process upsets and exigencies in the upstream sulfur removal processes or fluctuations in feed sulfur content, which may cause temporary H₂S spikes in the feed to the reformer.

* Corresponding author: Fax: +65 6779 1936.

E-mail address: chekawis@nus.edu.sg (S. Kawi).

¹ Authors contributed equally.

Metal catalysts, that are generally used for DRM, are known to be highly susceptible to sulfur poisoning due to the strong adsorption of sulfur on the metal surface and the formation of inactive metal sulfides [16]. Both noble metals and non-precious transition metals deactivate rapidly in the presence of H_2S [11,12,17]. For example, Mancino et al. [11] studied the effects of H_2S (1–30 ppm) on a $\text{Rh}/\gamma\text{-Al}_2\text{O}_3$ catalyst during biogas dry reforming and observed that the catalyst activity dramatically decreased by 90% of its original value within 7 min of being exposed to 20 ppm H_2S . Even at a low concentration of 1 ppm, H_2S severely poisoned the catalyst. Similarly, Theofanidis et al. [12] observed that exposure of a series of $\text{NiRu}/\text{MgAl}_2\text{O}_4$ catalysts to 7 ppm H_2S during dry reforming at 900 °C resulted in a 90% drop in methane conversion, whereas $\text{Ni}/\text{MgAl}_2\text{O}_4$ lost 98% of its activity under the same conditions. Ni/YSZ and $\text{Ni}/\text{K}_2\text{O}-\text{CaAl}_2\text{O}_4$ catalysts were also observed to get almost completely deactivated within 1 h in 5 ppm H_2S during DRM at 750 °C [13].

Ni is the most commonly investigated catalyst for DRM, primarily because of its lower cost and high catalytic activity in methane reforming [1,7]. However, compared to noble metal catalysts, Ni tends to form more coke under dry reforming conditions, making catalyst stability and coke resistance a primary concern for Ni-containing catalysts. Because of the high tendency to chemisorb sulfur, Ni-containing catalysts are also more prone to deactivation by H_2S than noble metals and are less likely to recover activity upon cessation of H_2S in the feed [12,18]. The presence of H_2S in the feed has also been observed to further accelerate the coke formation on the catalyst by poisoning sites for coke gasification reaction [11,17,19]. Thus, both chemisorption of sulfur on metal sites and fouling by promoted deposition of coke contribute to the rapid catalyst deactivation in H_2S -containing feed in DRM [17,20]. Some studies have reported that the catalytic activity may be partly recovered at high temperatures (>800 °C) upon stopping sulfur in the feed by the gradual desorption of sulfur [17,21], whereas other studies report permanent deactivation [20]. Calcination in an oxidative atmosphere is often required to remove the adsorbed sulfur by oxidation and regenerate the active Ni sites [20].

Thus, there is a need to develop catalysts for DRM that can resist instant or permanent deactivation upon exposure to H_2S -containing feed. Some sulfur tolerant catalysts have been attempted for DRM in recent years. For example, $\text{NiMo}/\gamma\text{-Al}_2\text{O}_3$ was reported to be stable in the presence of H_2S due to a lower tendency to adsorb H_2S ; however, the NiMo catalyst is poorly active for DRM, with the CH_4 conversion reaching a steady state value of barely 11% at 750 °C [22]. Some studies have reported an increase in the duration of H_2S exposure before the deactivation of Ni-based catalysts by the addition of noble metals [12, 23] or second transition metals like Co [24,25], or the addition of promoters such as ZrO_2 [24], etc. However, further improvement is needed in H_2S tolerance, in terms of the (i) time delay between H_2S exposure and onset of catalyst deactivation, (ii) steady state catalytic activity/DRM conversion in the presence of H_2S after catalyst deactivation, and (iii) ease of regeneration of catalytic activity upon cessation of H_2S in feed. At the same time, it is crucial that the sulfur-tolerant catalyst does not form coke, because coke-resistance is the primary requirement for long term DRM operation. So far, there are scarce reports of any catalyst that shows reasonable sulfur tolerance and anti-coking properties in DRM, while also having high catalytic activity.

One of the main advantages of core-shell catalysts is that they can combine materials that have various functionalities while being in close proximity to each other, thereby creating a bi-functional composite suited to address multiple problems [26]. The objective of this study is to develop a core-shell Ni-containing catalyst for DRM that has high resistance to coking, high catalytic activity, and, simultaneously, reasonable tolerance to H_2S impurity in the feed. In our previous reports, we showed that adding a layer of redox CeO_2 shell on Ni/SiO_2 catalysts to form a sandwiched core-shell structure helped in almost complete suppression of coke formation in DRM [27,28]. However, despite the high coke resistance of our reported $\text{Ni}/\text{SiO}_2 @\text{CeO}_2$ catalysts, they

exhibit poor tolerance to H_2S . In this work, we develop sandwiched core-shell catalysts with a layered double hydroxide (LDH) derived NiCoMgAl mixed oxide core and a redox-active CeO_2 shell, with an aim of achieving resistance to both coke and sulfur-induced deactivation in DRM. LDH or hydrotalcite-like materials containing Mg, Al and Ni have been studied extensively as catalyst precursors because of their unique physicochemical properties such as large surface area, tuneable acid/base properties, high homogeneity, thermally stable dispersion of metal ion components, etc. [29]. NiMgAl LDH derived catalysts have been reported to have high activity for DRM because of high and uniform Ni dispersion and acid/base properties of the $\text{MgO}-\text{Al}_2\text{O}_3$ oxide support [30,31]. Mg-Al containing LDH derived oxides have also been reported to be active in selective H_2S oxidation processes [32,33]. Hence, in this study, core-shell catalysts are synthesized using CeO_2 shell on a Ni-containing Mg-Al LDH core. After establishing the coke resistance of the core-shell catalyst under extended testing in DRM, the sulfur tolerance of the catalyst in the presence of trace amounts of H_2S (20 ppm) is investigated. The catalysts are thoroughly characterized by HRTEM, XRD, TPR, O_2 -TPD, CO_2 -TPD, BET, XPS, TPO, and Raman; and the role of the redox CeO_2 shell on the coke-resistance and sulfur tolerance of the core-shell catalyst is elucidated through detailed spent catalyst characterization and *in situ* DRIFTS experiments. The beneficial effect of modification of the NiMgAl LDH core by adding Co on the H_2S tolerance of the catalyst is also investigated.

2. Experimental

2.1. Catalyst synthesis

Ni-MgAl and NiCo-MgAl catalysts were synthesized via a layered double hydroxide (LDH) precursor route reported before [34]. An appropriate amount of the metal salts ($\text{Ni}(\text{NO}_3)_2 \cdot 0.6 \text{H}_2\text{O}$, $\text{Mg}(\text{NO}_3)_2 \cdot 0.6 \text{H}_2\text{O}$, $\text{Al}(\text{NO}_3)_3 \cdot 0.9 \text{H}_2\text{O}$ and $\text{Co}(\text{NO}_3)_2 \cdot 0.6 \text{H}_2\text{O}$) were added to an equimolar solution of ethanol and deionized water (60 ml), followed by addition of urea (1.2 g) and citric acid (0.23 g). The molar ratio of Ni, Co, Mg and Al nitrate salts was kept at 0.3/0/1.7/1 for Ni-MgAl and 0.3/0.3/1.7/1 for NiCo-MgAl . The solution was subjected to a hydrothermal treatment at 160 °C for 48 h, followed by centrifuging, washing, and drying at 100 °C overnight to obtain the solid NiMgAl and NiCoMgAl LDH materials. The LDH materials were calcined at 600 °C in air for 4 h to form Ni-MgAl and NiCo-MgAl mixed oxides. The calcination temperature was set at 600 °C to ensure complete removal of nitrate and organic components in the dried samples (based on a thermogravimetric analysis of the dried samples in air; details are provided in Supporting Information, Fig. S1).

Ni-MgAlCe was synthesized by the same process by adding Ce (NO_3)₃·0.6 H_2O to the synthesis solution, with the molar ratio of Ce: ($\text{Ni}+\text{Mg}+\text{Al}$) = 0.25.

Core-shell $\text{Ni-MgAl}@ \text{CeO}_2$ and $\text{NiCo-MgAl}@ \text{CeO}_2$ catalysts were synthesized by loading a solution of $\text{Ce}(\text{NO}_3)_3 \cdot 0.6 \text{H}_2\text{O}$ on the uncalcined NiMgAl and NiCoMgAl LDH cores by incipient impregnation. The impregnation step was repeated multiple times with intermediate vacuum drying at 100 °C to achieve a molar ratio of Ce: ($\text{Ni}+\text{Mg}+\text{Al}$) = 0.25. The quantity of Ce was set to completely coat the mixed oxide core. The dried sample was calcined at 600 °C for 4 h.

Catalyst reduction was conducted at 800 °C for 1 h in a flow of pure H_2 .

2.2. Catalyst characterization

The morphology of the catalysts was characterized by SEM, taken on a JOEL JSM-6700 F Field emission scanning electron microscope, and HRTEM taken on a JEOL JEM-2100 microscope operated at an acceleration voltage of 200 kV. Elemental mapping was done by coupling Energy dispersive X-ray (EDX) with HRTEM. XRD characterization was conducted on a Shimadzu XRD-6000 diffractometer using $\text{Cu K}\alpha$ as the

X-ray source in the 2θ range of $5\text{--}80^\circ$ at a scanning speed of $2^\circ/\text{min}$. An ASAP 2020 instrument was used to conduct nitrogen adsorption-desorption isotherms at 77 K for the measurement of specific surface area by the BET method and pore volume by BJH method. Samples were degassed prior to analysis by heating the catalyst at 300°C under vacuum ($500\ \mu\text{mHg}$). The elemental composition of the fresh catalysts was measured by ICP-OES (Thermo Scientific iCAP 6000). The sample was digested in a mixture of HNO_3 , HF , H_2O_2 and deionized water under ultrasonication before analysis.

To characterize the reducibility of the catalyst, H_2 -TPR of the fresh catalysts was performed on a Thermo Scientific TPDRO 1100 apparatus equipped with a thermal conductivity detector (TCD). 30 mg catalyst sample was heated in 5% H_2 in N_2 gas mixture at a $10^\circ\text{C}/\text{min}$ temperature ramping rate from 50°C to 900°C . H_2 pulse chemisorption was conducted on the same instrument to quantify metal surface. The catalyst was reduced for 1 h at 800°C in 5% H_2 - N_2 and subsequently cooled under N_2 flow to 30°C and treated with 10 pulses of H_2 of known volume. The moles of H_2 chemisorbed was used to calculate the moles of surface nickel/nickel-cobalt assuming an adsorption stoichiometry of 1. O_2 -TPD was performed in the same apparatus, wherein, the catalyst was first reduced for 1 h in 5% H_2 - N_2 followed by cooling to 700°C in He, flowing O_2 at 700°C for 1 h, cooling to 50°C in O_2 flow, and purging with He. The temperature was then ramped under He flow from 50°C to 850°C , and the product was continuously analysed by a Shimadzu gas chromatograph mass spectrometer (GCMS-QP2010). For CO_2 -TPD, a fixed weight of catalyst was reduced in 5% H_2 - N_2 followed by cooling under inert atmosphere to 50°C . The catalyst was then saturated with CO_2 by flowing 30 ml/min CO_2 for 1 h at 50°C . The residual CO_2 was purged by flowing helium and the temperature ramping was done under He flow from 50°C to 950°C .

X-ray photoelectron spectroscopy (XPS) of the catalysts was conducted on a Kratos AXIS Ultra DLD using an Al $K\alpha$ X-ray source (1486.6 eV). Samples were exposed to air during sample preparation for XPS. C1s reference signal was calibrated to 284.5 eV.

The amount of carbon residue on the spent catalyst after DRM reaction was measured by thermo-gravimetric analysis (TGA) coupled with DTA (differential thermal analysis) on a Shimadzu DTG-60 thermogravimetric analyser by heating a fixed weight of spent catalyst in static air to 850°C at $10^\circ\text{C}/\text{min}$ ramp rate. Raman spectra of the spent catalysts were obtained on a Xplora Plus Microscope Raman (HORIBA, Japan) with a grating of 600 gr/mm equipped with a 638 nm laser beam. Temperature-programmed oxidation (TPO) of the spent catalysts after DRM with H_2S containing feed was conducted in a quartz reactor placed in a Carbolite furnace. The used catalyst was heated in flowing air (10 ml/min) at a rate of $5^\circ\text{C}/\text{min}$, and the product was continuously analysed by a Shimadzu gas chromatograph mass spectrometer (GCMS-QP2010).

2.3. Catalyst evaluation

For catalytic testing of DRM reaction, a micro-catalytic reactor system in a single pass, steady-state plug flow mode was employed. In each test, the catalyst (50 mg) without any dilution was packed in a 4 mm quartz tube, positioned in a Carbolite furnace. The catalyst was reduced under 20 ml/min of pure H_2 at 800°C for 1 h. A controlled flowrate of the feed-gas was introduced into the reactor using mass flow controllers. For testing the coke tolerance of catalysts, DRM was conducted at 600°C , 1 bar pressure, CH_4 : CO_2 : He ratio of 1:1:1, total gas flowrate of 30 ml/min, and a WHSV (based on total gas flow rate) of $36\ \text{Lh}^{-1}\text{g}^{-1}$. The effluent product from the reactor was passed through a cold trap to condense water, and the non-condensable product gases were analysed with an online Agilent 7820 A gas chromatograph equipped with a Hayesep D column.

H_2S tolerance of the catalysts was tested at 800°C , 1 bar pressure, CH_4 : CO_2 : He ratio of 1:1:2.5, total gas flowrate = 45 ml/min, WHSV of $54\ \text{Lh}^{-1}\text{g}^{-1}$ and 20 ppm H_2S . After reduction, DRM was conducted for

1 h without H_2S , followed by flowing H_2S for 18 h. After that, H_2S was stopped and the catalyst activity recovery over time in DRM was monitored.

2.3.1. In situ DRIFTS during DRM

In situ DRIFTS was conducted in a Bruker FTIR Vertex 70 spectrometer using a Harrick Praying Mantis DRIFTS gas cell. Ni-MgAl@CeO₂ was reduced at 800°C for 1 h *ex situ* and then again reduced *in situ* in the DRIFTS cell at 600°C . Background spectra were collected at 600°C in flowing helium. Pulses of the reactant gases (CH_4 and CO_2) were introduced in the sequence of $\text{CH}_4 \rightarrow \text{CO}_2 \rightarrow \text{CH}_4$ with continuous He flow at 10-minute intervals. Time resolved DRIFTS spectra were collected every 15 s (repeated 64 times, resolution of $4\ \text{cm}^{-1}$).

2.3.2. Identification of sulfur-containing products during H_2S and CO_2 flow

To examine the formation of sulfur-containing products when H_2S is present in the reactant stream along with CO_2 , the NiMgAl@CeO₂ catalyst (100 mg) was loaded in a quartz reactor with the outlet stream connected to an online mass spectrometer (GCMS-QP2010). The catalyst was reduced in H_2 (20 ml/min) at 800°C for 1 h. The reactor was then purged with helium, followed by introduction of H_2S (300 ppm, balance He) at 800°C . After 40 min, the flow of H_2S was stopped, and 10% CO_2 (balance He) was introduced into the reactor. After 45 min, a mixture of H_2S (300 ppm) and CO_2 (10%) in helium was introduced, while maintaining reactor temperature at 800°C . The outlet gas was continuously monitored by the mass spectrometer.

A control experiment was conducted using CeO₂ as the catalyst. 200 mg of CeO₂ was loaded in the quartz reactor and treated in H_2 (20 ml/min) at 800°C for 1 h. After purging the reactor with helium, a mixture of H_2S (300 ppm) and CO_2 (10%) in helium was introduced, while maintaining reactor temperature at 800°C . The outlet gas was continuously monitored by the mass spectrometer.

3. Results and discussion

3.1. Fresh catalyst characterization

3.1.1. Catalyst morphology

The morphology of the catalysts was observed by SEM and HRTEM. SEM images of the as-prepared NiMgAl LDH (Fig. 1a) show flower-like microspheres of diameter around 2.5 μm , composed of hierarchically arranged nanosheets of thickness between 20 and 30 nm. The thin nanosheet morphology is characteristic of the lamellar LDH structure. SEM and HRTEM images (Fig. S2a, and Fig. 1b respectively) of the calcined Ni-MgAl catalyst shows that the nanosheet assembled 3D flower-like morphology remains unchanged by the calcination process. The calcined NiCo-MgAl catalyst also shows a similar hierarchical nanoflower morphology (Fig. 1d).

H_2 -reduction of the calcined Ni-MgAl and NiCo-MgAl mixed oxide catalysts leads to the reduction of nickel and cobalt ions in the mixed oxide and the formation of Ni and NiCo nanoparticles, respectively, supported on MgO-Al₂O₃ mixed oxide. Uniform Ni nanoparticles of size $9.1 \pm 1.4\ \text{nm}$ and NiCo nanoparticles of size $9.3 \pm 1.6\ \text{nm}$ are observed in the reduced Ni-MgAl and NiCo-MgAl, respectively (Fig. 1c, e and Fig. S3).

HRTEM images of the calcined Ni-MgAl@CeO₂ and NiCo-MgAl@CeO₂ catalysts (Figs. 1g and 1i, respectively) show a dense layer on the mixed oxide microspheres, which corresponds to the CeO₂ shell. It can be observed from a comparison of the HRTEM micrographs of Ni-MgAl and Ni-MgAl@CeO₂ that the nanosheets composing the Ni-MgAl spheres are completely covered in Ni-MgAl@CeO₂. Fig. 1h shows a higher magnification image of the highlighted section in Fig. 1g, wherein, nanocrystals of cerium oxide (identified from characteristic lattice spacing, Fig. S4) can be seen to be superimposed on the underlying LDH-derived mixed oxide nanosheets. The core-shell structure with the Ni-MgAl core and CeO₂ shell is clearly characterized by EDX mapping of

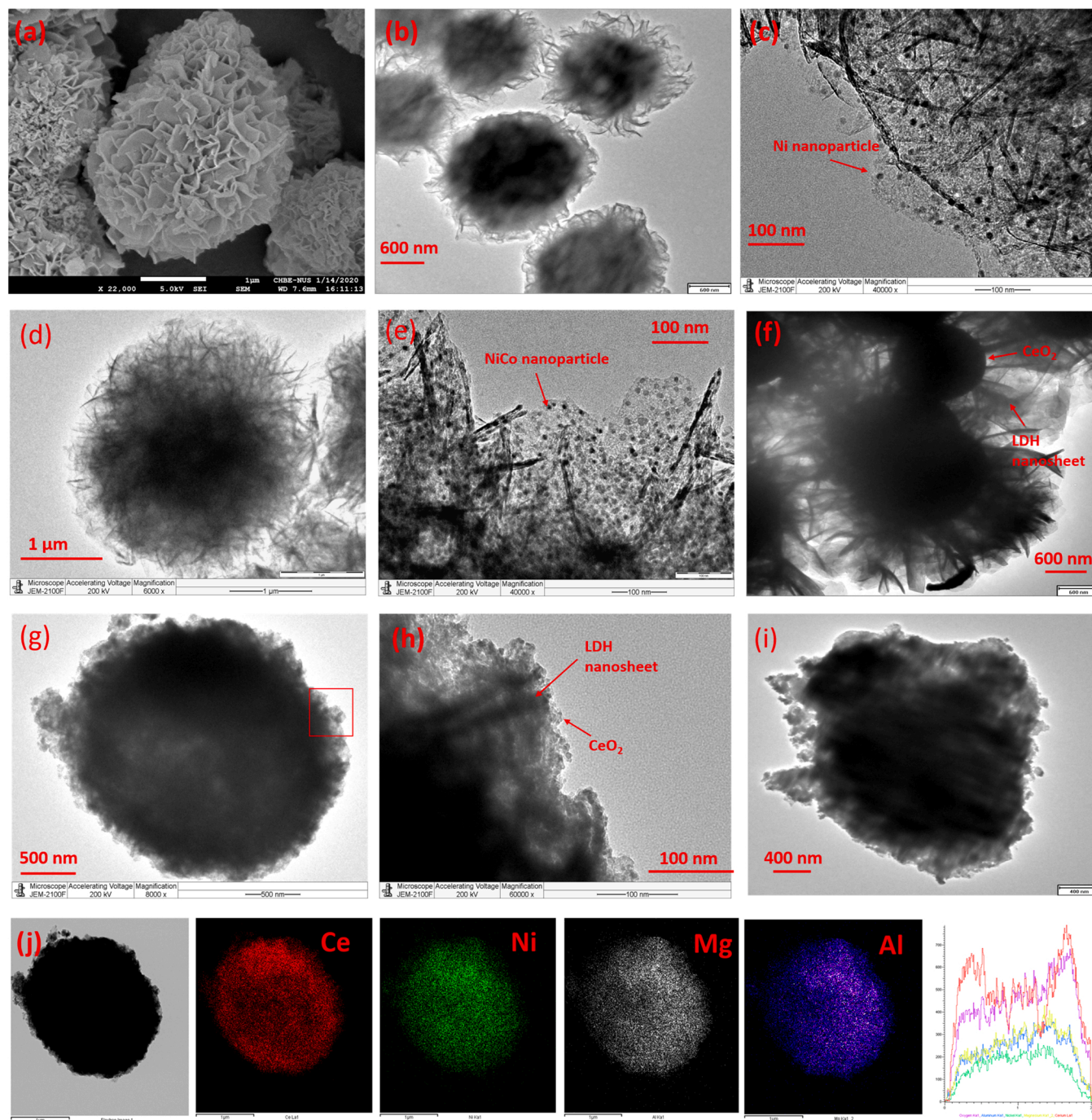


Fig. 1. (a) SEM of uncalcined NiMgAl LDH; HRTEM image of (b) calcined Ni-MgAl, (c) reduced Ni-MgAl, (d) calcined NiCo-MgAl, (e) reduced NiCo-MgAl, (f) calcined Ni-MgAlCe, (g, h) calcined Ni-MgAl@CeO₂, (i) calcined NiCo-MgAl@CeO₂, (j) EDX mapping of calcined Ni-MgAl@CeO₂.

the sample, which shows a higher intensity of Ce towards the edges of the sphere, whereas Al, Ni and Mg are concentrated in the core (Fig. 1j). Fig. 1j also shows a line scan profile of Ce, Al, Ni and Mg across the core-shell catalyst. Ce intensity is maximum at the edges and declines to form a valley towards the centre, whereas Ni, Mg and Al have higher intensity in the centre and less at the edges. A schematic representation of the sandwiched core-shell structure of the Ni(Co)-MgAl@CeO₂ catalyst after reduction is shown in Scheme S1 in Supporting Information. We point out that the LDH nanosheets composing the flower-like core of the catalyst act as scaffolds for the deposition of CeO₂ crystals that constitute the shell. The characteristic lamellar structure of LDH is important for ensuring sufficient interface between the mixed metal oxide and the

CeO₂ shell, which is deposited on the extended external surface of the nanosheet substrate. Since the deposited CeO₂ crystals (estimated to be 3 – 4 nm from HRTEM images, Fig. S4) are smaller than the inter-lamellar voids of these LDH nano-sheets (Table 1), penetration of CeO₂ into these voids in the core is possible. Such penetration of CeO₂ into the inter-lamellar voids of the LDH core is desirable because it is consistent with our aim of synthesizing a sandwiched core-shell structure where all exposed surface of the LDH-derived mixed oxide nano-sheets is covered by a porous CeO₂ overlayer.

A reference Ni-MgAlCe catalyst was prepared by one-pot hydrothermal synthesis, following the same procedure as that of the NiMgAl LDH synthesis, and including appropriate amount of cerium precursor in

the synthesis solution. It was observed from SEM (Fig. S2b) that a mixture of cerium oxide nanospheres and NiMgAl LDH spheres are formed by this method, each forming a distinct and separate phase and structure. There was no indication of incorporation of Ce ions inside the LDH structure, which agrees with previous reports of Ce promoted LDH derived catalysts, where CeO₂ was always observed to form a separate phase instead of being incorporated inside the LDH lattice [35,36]. Both HRTEM (Fig. 1f) and SEM (Fig. S2b) images indicate that the ceria and the LDH-derived mixed oxide components are randomly distributed with limited interaction and no core-shell morphology in the Ni-MgAlCe sample prepared by the one-pot synthesis.

3.1.2. Crystal structure

The formation of the hydrotalcite or LDH phase in the uncalcined NiMgAl and NiCoMgAl precursors were confirmed from the XRD patterns of the fresh samples before calcination (Fig. S5). The structure of LDH or hydrotalcite compounds is similar to that of brucite Mg(OH)₂ and may be represented by the general formula $[M^{2+}_x M^{3+}_y (OH)_2]^{x+y}(A^{n-})^{x/n} \times mH_2O$, where M^{2+} and M^{3+} represents divalent and trivalent cations, and A^{n-} represents interlayer charge-balancing anion [37]. The XRD pattern of the uncalcined NiMgAl sample (Fig. S5) shows diffraction peaks at $2\theta = 7.3, 14.7, 22, 35, 39.5, 47.4$ and 61.1° that can be indexed to the (003), (006), (009), (012), (015), (018) and (110) planes of the characteristic LDH phase with the intercalation of citrate ligands in the inter-layer gallery of the LDH [34,38]. The XRD pattern of the uncalcined NiCoMgAl sample shows diffraction peaks at $2\theta = 11.4, 23.1, 34.9, 39.4, 46.8, 60.9$ and 62° , corresponding to LDH structure with carbonate anion in the inter-layer [39]. The intercalated anions in the LDH structure can be easily exchanged, depending upon the pH and concentration of the anions in solution, and the difference in the anion intercalation in the LDH between NiMgAl and NiCoMgAl is likely caused by changes in solution composition and pH caused by cobalt nitrate addition. However, in both the catalysts, pure LDH phase is formed and no additional peak corresponding to metal oxide phases (NiO, Co₂O₃) are observed, indicating the successful incorporation of Ni²⁺ and Co²⁺ cations into the brucite layers of LDH structures.

Air calcination of the LDH materials at high temperature leads to the collapse of the hydrotalcite structure, removal of the interlayer anions, and the formation of a mixed metal oxide phase with a periclase structure [39]. XRD of the Ni-MgAl and NiCo-MgAl samples after calcination (Fig. 2a) show diffraction peaks at $2\theta = 35.3, 43.2$ and 62.8° , similar to that of MgO periclase. Reflections corresponding to the MgAl₂O₄ spinel phase are not observed, indicating that the spinel phase is either poorly crystalline or below the detection limit of XRD. Similarly,

NiAl₂O₄, CoAl₂O₄ spinel phases are not detected in the calcined catalysts by XRD.

The XRD pattern of the calcined Ni-MgAlCe catalyst synthesized by one pot method show reflections for the fluorite type CeO₂ phase at $2\theta = 28.6, 33.1, 47.5, 56.4, 59.4, 69.6^\circ$ and the periclase type mixed metal oxide discussed above. The presence of distinct diffractions for the CeO₂ fluorite structure show that Ce is not incorporated inside the lattice of the mixed metal oxide and exists as a separate phase. Previous studies of Ce doped hydrotalcite derived mixed metal oxide catalysts also reported separate phase formation of ceria, because of the higher ionic radius of Ce [35,36]. Similarly, the XRD patterns for the calcined core-shell Ni-MgAl@CeO₂ and NiCo-MgAl@CeO₂ catalysts show peaks for both periclase mixed oxide and fluorite CeO₂, with no evidence of Ce incorporation in the MgAl-mixed metal oxide. Compared to the core Ni-MgAl and NiCo-MgAl, the diffraction peaks corresponding to the periclase structure is significantly attenuated in the XRD spectrum of ceria containing catalysts. The attenuation of peak intensity may be caused by a combination of factors such as the lower weight fraction of periclase mixed metal oxide in these catalysts, the X-ray scattering properties of CeO₂ and a possible loss in crystallinity of the periclase core during core-shell catalyst synthesis.

XRD pattern of all the catalysts after reduction (Fig. 2b) exhibits characteristic peaks for metallic Ni or NiCo alloy along with the periclase oxide and CeO₂ peaks. The diffraction peaks for face centred cubic (fcc) phase of Ni are observed to shift to lower angles in the XRD pattern of the reduced NiCo-MgAl sample compared to that of Ni-MgAl (Fig. S6). This indicates an increase in the lattice parameter of Ni, which is consistent with the formation of NiCo alloy with fcc structure. The composition of the NiCo alloy in NiCo-MgAl was estimated from the calculated lattice parameter using Vegard's law to be approximately Ni_{0.45}Co_{0.55}, which is close to the stoichiometric value (Table S1). Formation of NiCo alloy is also expected for the core-shell NiCo-MgAl@CeO₂; however, it is difficult to discern the exact angles of the diffraction peaks for metallic nickel or the alloy in the XRD patterns of the reduced core-shell materials.

3.1.3. Reducibility

Ni 2p XPS analysis of the calcined samples (Fig. S7a) indicates that nickel is present as Ni²⁺, evidenced from the Ni 2p_{3/2} peak in the range of 855.5 – 855.8 eV with a satellite peak around 861.5 eV. There is no evidence of metallic Ni⁰ in the calcined samples. Likewise, cobalt is present in oxidized state in the calcined samples, with the position of the Co 2p_{3/2} peak of NiCo-MgAl and NiCo-MgAl@CeO₂ (780.5 – 780.6 eV) being similar to that of Co²⁺ in CoO (Fig. S8a). The +2 oxidation state of both Ni and Co is consistent with the incorporation of Ni and Co in the periclase structure of the mixed-metal oxide, as observed by XRD. The intensity of Ni 2p and Co 2p peaks is much lower on the core-shell Ni-MgAl@CeO₂ and NiCo-MgAl@CeO₂ samples than on Ni-MgAl and NiCo-MgAl, which is expected because of lower surface concentration of Ni/Co in the core-shell structure.

The reducibility of Ni and Co in the catalysts was probed by H₂-TPR. The H₂-TPR profile of Ni-MgAl exhibits a single peak for the reduction of Ni²⁺ to Ni⁰ centred at 740 °C (Fig. 3a). The high temperature of the TPR peak agrees well with the reduction of Ni²⁺ in a mixed metal oxide solid solution [31,36]. The absence of any significant peak at lower temperatures shows the uniformity of the chemical state of all Ni species in the sample and the absence of nickel oxide phase or any Ni species with weak interaction with the support. The main reduction peak is shifted to slightly lower temperature (710 °C) in the NiCo-MgAl catalyst, which can be attributed to the formation of NiCo alloy. In bimetallic NiCo catalysts, the formation of NiCo alloy has been proposed to moderate the interaction with the support and increase the reducibility of Ni [40]. A broad low temperature peak in the temperature range of 200 – 400 °C is also observed and may be assigned to the partial reduction of small amount of cobalt oxide phase, that is not detectable by XRD.

In both the Ni-MgAl@CeO₂ and NiCo-MgAl@CeO₂ core-shell

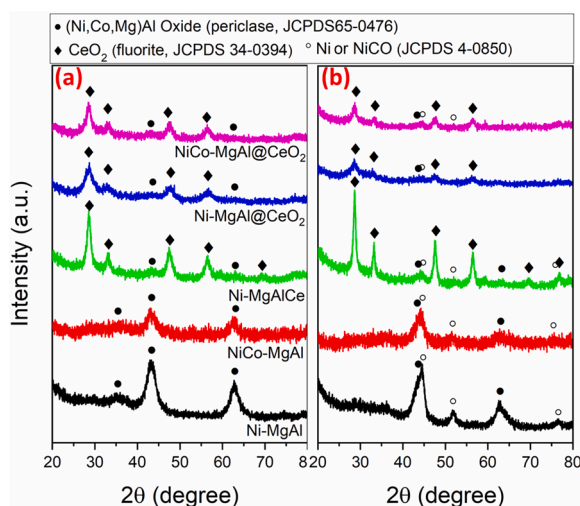


Fig. 2. XRD patterns of (a) calcined and (b) reduced catalysts.

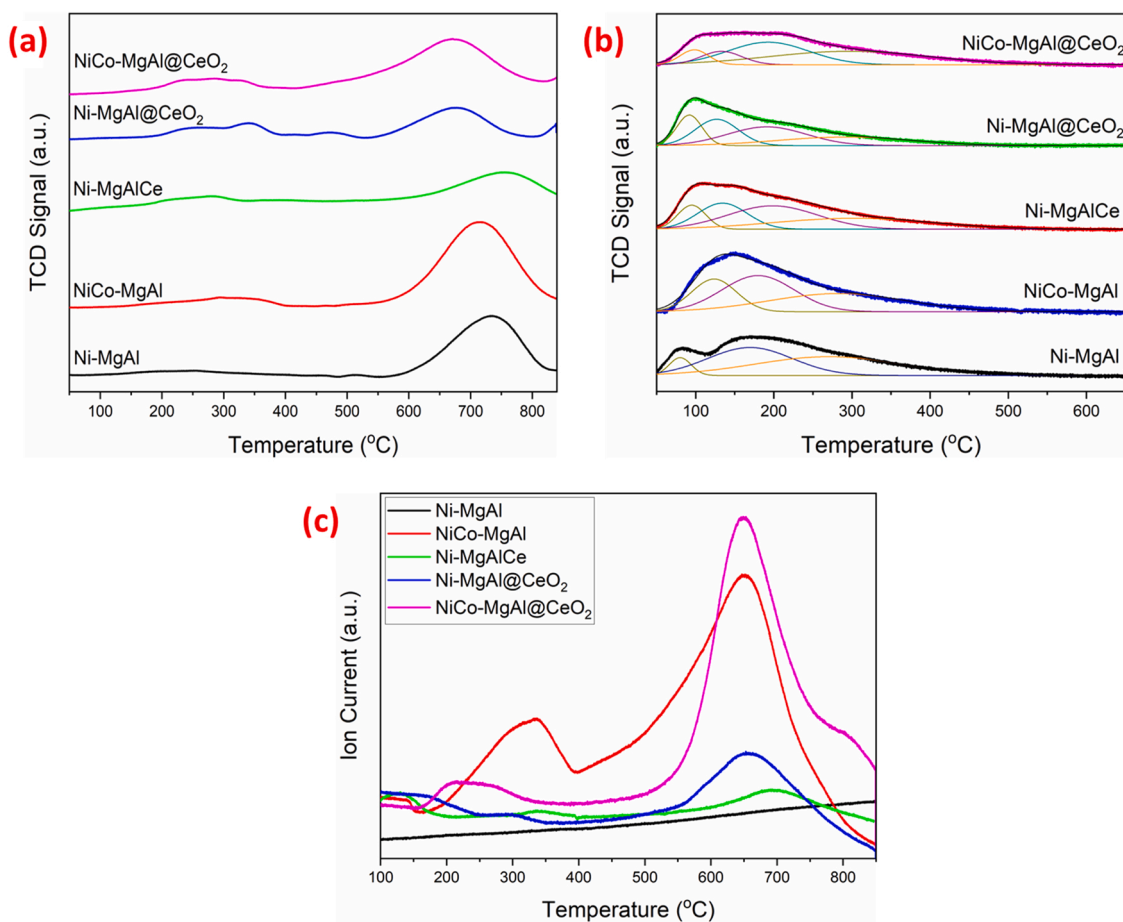


Fig. 3. (a) H₂-TPR, (b) CO₂-TPD, and (c) O₂-TPD profiles of catalysts.

catalysts, the reduction temperature of Ni is further reduced to 670 – 680 °C, because of its interaction with CeO₂. The promotional effect of cerium oxide on the reducibility of metals in neighbouring areas by virtue of its redox nature is well documented in literature [27,31]. In comparison, the Ni-MgAlCe catalyst synthesized by the one-pot hydrothermal method does not show a similar decrease in reduction temperature, reaffirming the lack of interaction between Ni and ceria in this catalyst. The TPR profiles of all the CeO₂ containing catalysts exhibit an additional small peak in between 200 and 300 °C, which is attributed to the surface reduction of Ce⁴⁺ to Ce³⁺ and of chemisorbed oxygen species adsorbed on the oxygen vacancies in the cerium oxide lattice.

The reduction temperature for activation of the catalysts before reaction was fixed at 800 °C based on the H₂-TPR results. Ni 2p and Co 2p XPS spectra of the samples after reduction at 800 °C (Fig. S7b and S8b, respectively) give evidence of the formation of metallic Ni⁰ and Co⁰ after reduction (note that the reduced samples were air-exposed before XPS analysis, and the appearance of Ni²⁺ peaks in the XPS spectra may be a resultant artifact).

3.1.4. Textural analysis

All the calcined catalysts exhibited N₂ adsorption-desorption isotherms of type IV, typical of mesoporous materials. The Ni-MgAl and NiCo-MgAl catalysts are characterized by a high BET surface area of 162 m²/g (Table 1), which is characteristic of the LDH precursor [41, 42]. The BET surface area, pore volume and average pore size is lower on the core-shell Ni-MgAl@CeO₂ and NiCo-MgAl@CeO₂ catalysts compared to the mixed oxide cores. The decreased specific surface area and pore volume is related to the partial coverage of the porous nano-sheet structure and partial blockage of the mesopores by CeO₂ nanocrystals. The reference Ni-MgAlCe catalyst synthesized by one-pot

Table 1
Textural properties of calcined catalysts.

Catalyst	S _{BET} (m ² g ⁻¹)	V _{pore} ^a (cm ³ g ⁻¹)	d _{pore} ^b (nm)
NiCo-MgAl	161.8	0.564	21.6
Ni-MgAlCe	101.2	0.391	20.8
Ni-MgAl@CeO ₂	127.9	0.128	4.9
NiCo-MgAl@CeO ₂	98.4	0.186	6.7

^a BJH desorption pore volume.

^b BJH desorption average pore diameter.

method also has lower specific surface area and pore volume than Ni-MgAl, attributed to the relatively lower specific surface area and porosity of the precipitated CeO₂ component in the catalyst compared to the NiMgAl mixed oxide [35]. However, the pore volume and average pore diameter in Ni-MgAlCe is higher than the core-shell Ni-MgAl@CeO₂ and NiCo-MgAl@CeO₂ catalysts, reflecting the difference in core-shell morphology.

3.1.5. CO₂-TPD analysis

The basicity of the catalysts was probed by temperature programmed desorption of CO₂ (Fig. 3b). The temperature of CO₂ desorption and amount of CO₂ desorbed are characteristic of the nature and concentration of basic sites, respectively. Both the Ni-MgAl and NiCo-MgAl materials exhibit three CO₂ desorption peaks during CO₂-TPD in the temperature range of 50 – 500 °C. The first desorption peak observed at temperature less than 150 °C is attributed to the desorption of CO₂ from weakly basic Brønsted surface hydroxyl groups, the peak observed at around 170 °C can be assigned to the formation of bidentate carbonates formed on metal-oxygen pairs with moderate basic strength, and the

CO₂ adsorbed on strong basic sites is desorbed at temperatures higher than 250 °C [43,44]. The amount of total basic sites on NiCo-MgAl is higher than Ni-MgAl (Table S2). At the same time, the CO₂ desorption temperature is higher for all the types of basic sites on NiCo-MgAl compared to Ni-MgAl, indicating higher basic strength. The addition of CeO₂ results in an additional CO₂ desorption peak in the low temperature range (< 150 °C), that may be assigned to weak basic sites on cerium oxide [45]. The small changes observed in the CO₂ desorption peak temperature of weak basic sites of the samples with and without Ce could be a result of interactions of the Ni/Co-MgAl oxide surface and CeO₂ surface, such as, physical blocking of some surface sites of Ni/Co-MgAl by CeO₂ or the modification of electronic properties of the surface sites. The peak temperatures for medium and strong basic sites are shifted to slightly higher values for the Ce containing samples. The overall basicity is observed to decrease in the order NiCo-MgAl > Ni-MgAlCe > Ni-MgAl > NiCo-MgAl@CeO₂ > Ni-MgAl@CeO₂ (Table S2).

3.1.6. O₂-TPD analysis

O₂-TPD was conducted to investigate the oxygen release properties of the catalysts. Negligible oxygen desorption was observed from Ni-MgAl (Fig. 3c). Both the Ni-MgAlCe and Ni-MgAl@CeO₂ catalysts showed a O₂ desorption peak at temperature > 600 °C, because of the release of lattice oxygen from CeO₂. The amount of O₂ desorbed is higher for the core-shell Ni-MgAl@CeO₂ than Ni-MgAlCe, because of better Ni-CeO₂ interaction, that helps in creating oxygen defects in CeO₂ and facilitates the partial reduction and oxygen release from CeO₂ [46]. The NiCo-MgAl catalyst shows distinct peaks of O₂ release

corresponding to the thermal reduction of Co oxides. Addition of CeO₂ to NiCo-MgAl in the core-shell NiCo-MgAl@CeO₂ catalysts is observed to increase the high temperature peak (> 600 °C) O₂ desorption, likely due to an overlap of O₂ released from CeO₂ and Co oxide reduction.

3.2. Evaluation of coke-resistance in DRM

3.2.1. Catalyst performance and stability

A low rate of coke formation is crucial for the long-term operation of dry reforming of methane or biogas. Hence the primary requirement for the catalyst is to be able to inhibit the formation of coke. In this section, the DRM performance of the catalysts in terms of activity and coke resistance is presented. The stability of the prepared catalysts was tested at 600 °C, because of the relatively higher thermodynamic potential for coke deposition at this temperature [47].

Fig. 4 shows the conversion of CH₄ and CO₂ and the H₂/CO ratio in the product from DRM at 600 °C (mole balances are provided in Fig. S9). The Ni-MgAl catalyst demonstrates CH₄ and CO₂ conversion of 57% and 63% at the start of the reaction. The observed CH₄ conversion is higher than the calculated equilibrium conversion when only CO and H₂ are considered as reaction products (equilibrium CH₄ conversion at the used reaction conditions is 49.5%) but lower than the calculated equilibrium conversion when surface carbon forming reactions are also considered [48] and coke is included as one of the products (equilibrium CH₄ conversion at the used reaction conditions including coke as a product is 84.8%). This indicates that there is some contribution of surface carbon forming reactions in the conversion of methane. CO₂ conversion is observed to be higher than CH₄ conversion because of the occurrence of

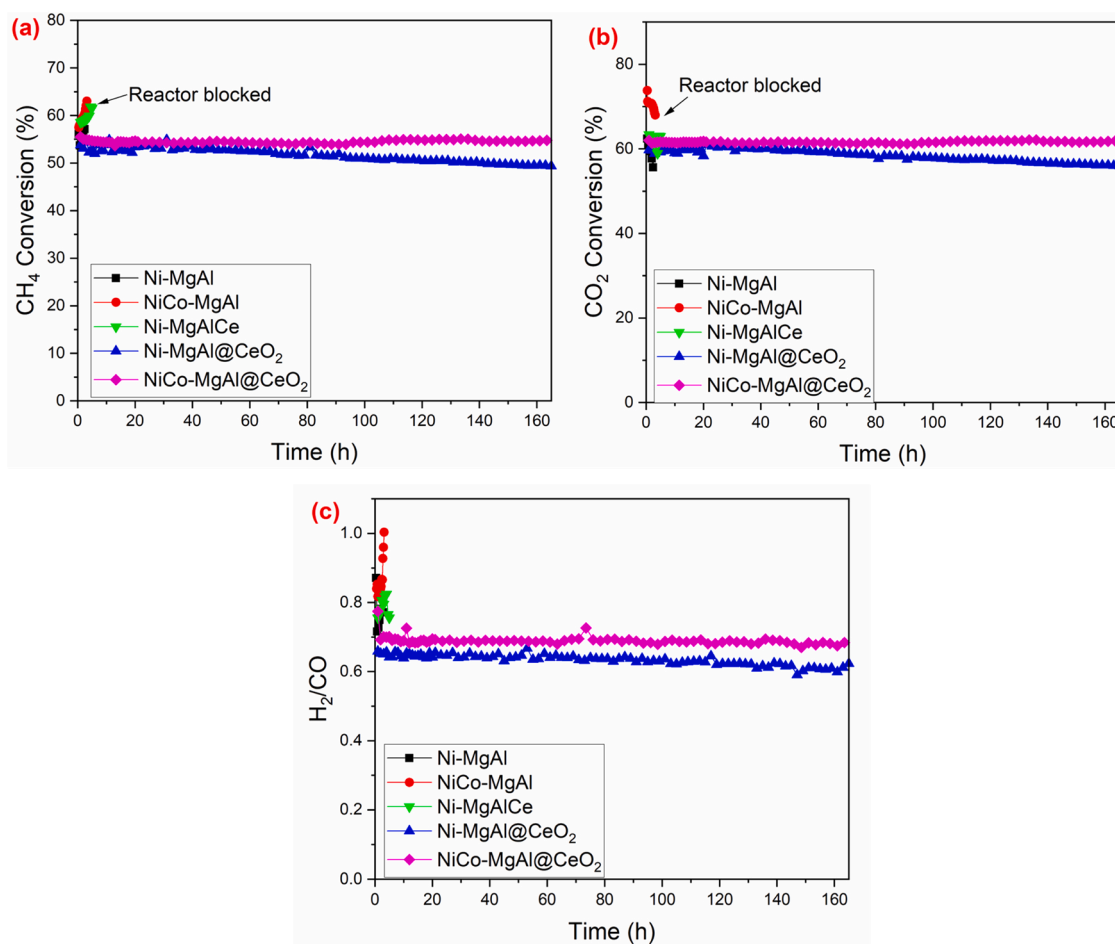


Fig. 4. Catalyst performance in DRM. Reaction conditions: Temperature = 600 °C, pressure = 1 bar, WHSV = 36 Lg⁻¹h⁻¹, CH₄/CO₂/He = 1:1:1 – (a) CH₄ conversion, (b) CO₂ conversion, (c) H₂/CO ratio.

RWGS. With time, the CH_4 conversion was observed to increase. This was accompanied by a pressure rise at the reactor inlet, caused by plugging of the catalyst bed by formation of coke. Eventually, the catalyst bed was completely blocked by coke at around 3 h onstream, preventing the reactants from entering the reactor. The reaction was stopped when the bed inlet pressure increased beyond 3.5 bars due to bed blockage.

The NiCo-MgAl catalyst showed similar behaviour as Ni-MgAl. CO_2 conversion on NiCo-MgAl was observed to be higher than on Ni-MgAl, possibly because of its higher basicity. CH_4 conversion and H_2/CO ratio over time increased over time, indicating that CH_4 decomposition to form carbon and H_2 increases with time onstream. The reactor was blocked by coke formation within 3.5 h onstream.

Ni-MgAlCe prepared by the one-pot synthesis also deactivated by blocking the reactor bed within 5 h, showing that the addition of Ce in the one-pot synthesis method was ineffective in suppressing coke formation. This is attributed to the poor interaction of Ce with Ni in this catalyst.

In contrast to the above catalysts, both the core-shell Ni-MgAl@ CeO_2 and NiCo-MgAl@ CeO_2 catalysts showed extremely stable performance in DRM, without any pressure build-up from coke deposition. The catalyst stability was tested for a week (165 h) on the core-shell catalysts, during which reactant conversion was observed to be stable, and reactor blockage was not observed. Conversion on the core-shell catalysts were slightly lower than that on the corresponding mixed oxide catalysts. A marginal decrease in CH_4 and CO_2 conversions over the Ni-MgAl@ CeO_2 (by c.a. 4% and 5.5%, respectively) was observed over the

165-h time onstream. Negligible deactivation was observed on NiCo-MgAl@ CeO_2 , with the CH_4 and CO_2 conversion remaining stable throughout the stability test.

3.2.2. Characterization of coke on spent catalysts

HRTEM micrographs of the used catalysts after the stability test in DRM at 600 °C provide evidence of the formation of coke during the reaction (Fig. 5). Extensive filamentous coke is observed in the HRTEM images of spent Ni-MgAl and NiCo-MgAl after DRM for 3 h. Some carbon nanotubes are observed to have metal nanoparticles at their tip (Fig. S10), showing the detachment of Ni/ NiCo nanoparticles from the support by tip-growth of filamentous coke. HRTEM images of the spent core-shell Ni-MgAl@ CeO_2 and NiCo-MgAl@ CeO_2 catalysts after DRM for 165 h also show some filamentous coke. However, the amount of these coke deposits can be visually seen to be far lower than that on the corresponding metal oxide catalysts.

The amount of coke on the used catalysts after the stability test in DRM at 600 °C was quantified by TG-DTA (Fig. 6a). The coke deposition rates on the various catalysts were calculated from the weight loss during oxidation of the spent catalysts in the TGA and follows the order of NiCo-MgAl ($0.31 \text{ g}_{\text{coke}}\text{g}_{\text{cat}}^{-1}\text{h}^{-1}$) \approx Ni-MgAl ($0.285 \text{ g}_{\text{coke}}\text{g}_{\text{cat}}^{-1}\text{h}^{-1}$) $>$ Ni-MgAlCe ($0.19 \text{ g}_{\text{coke}}\text{g}_{\text{cat}}^{-1}\text{h}^{-1}$) $>>$ NiCo-MgAl@ CeO_2 ($0.0023 \text{ g}_{\text{coke}}\text{g}_{\text{cat}}^{-1}\text{h}^{-1}$) \approx Ni-MgAl@ CeO_2 ($0.0022 \text{ g}_{\text{coke}}\text{g}_{\text{cat}}^{-1}\text{h}^{-1}$). The coke deposition rates on the core-shell catalysts are, thus, lower by almost two orders of magnitude than the other catalysts. This is consistent with the observations from HRTEM and clearly demonstrate the effectiveness of the core-shell catalysts in inhibiting coke formation in DRM.

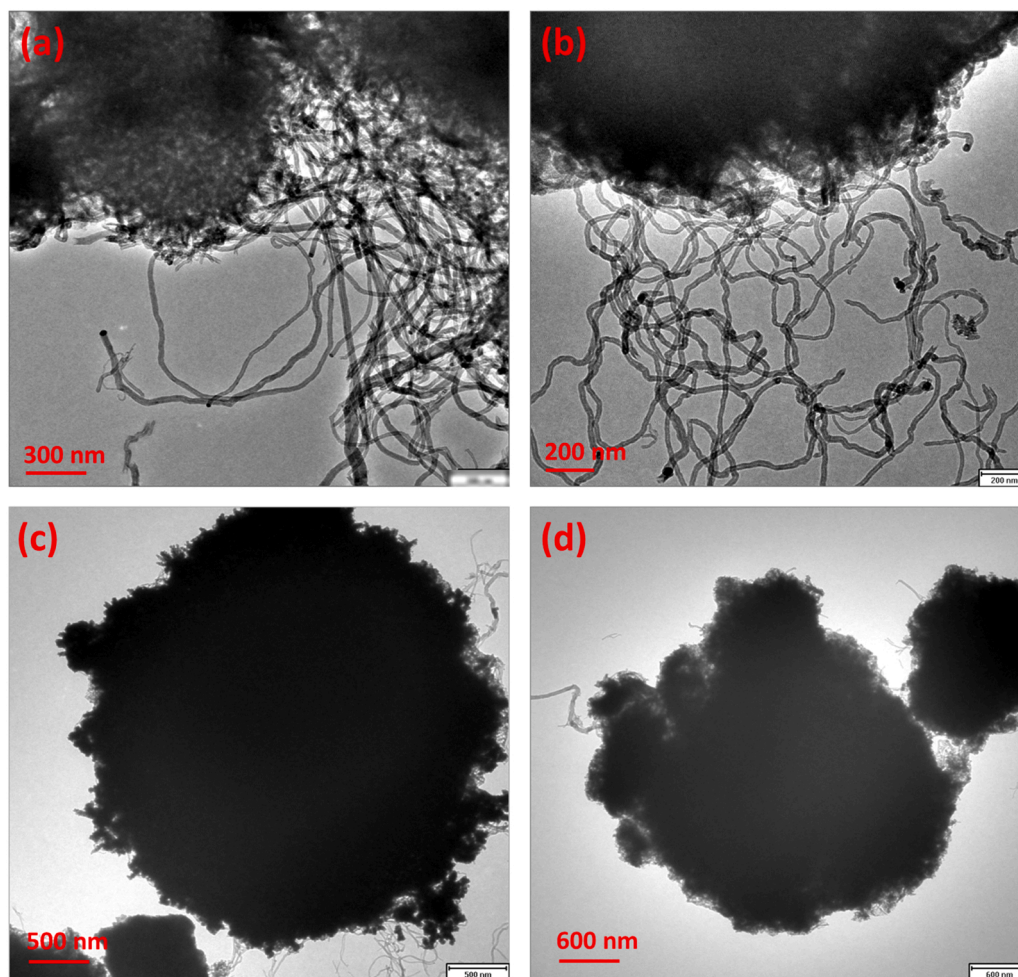


Fig. 5. HRTEM images of spent catalyst after DRM stability test (reaction conditions: temperature = 600 °C, pressure = 1 bar, WHSV = $36 \text{ Lg}^{-1}\text{h}^{-1}$, $\text{CH}_4/\text{CO}_2/\text{He} = 1:1:1$) – (a, b) Ni-MgAl and NiCo-MgAl, respectively, after 3 h onstream; (c, d) NiMgAl@ CeO_2 and NiCoMgAl@ CeO_2 , respectively, after 165 h onstream.

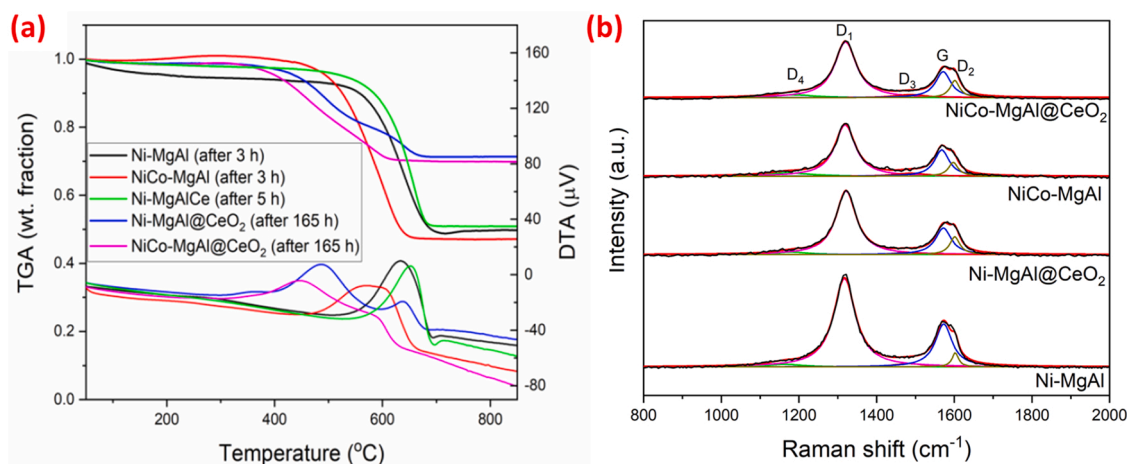


Fig. 6. (a) TG-DTA profiles and (b) Raman spectra of spent catalysts after DRM (reaction conditions: temperature = 600 °C, pressure = 1 bar, WHSV = 36 Lg⁻¹h⁻¹, CH₄/CO₂/He = 1:1:1).

The nature of coke was also observed to be different on the core-shell catalysts compared to the non-core-shell ones. TGA data for Ni-MgAl, NiCo-MgAl, and Ni-MgAl@CeO₂ show only one step of weight loss (with a corresponding DTA peak) starting at approximately 500 °C, which can be attributed to the combustion of inactive graphitized carbon, such as filamentous coke [49–51]. On the other hand, two distinct weight-loss steps are observed in the TG-DTA profiles of the spent core-shell Ni-MgAl@CeO₂ and NiCo-MgAl@CeO₂ catalysts – one starting at c.a. 300 °C, and another starting at > 500 °C. The low temperature weight loss may be attributed to oxidation of disordered or amorphous coke, that has been reported to be oxidized in the temperature range of 250 – 400 °C [49–51]. Thus, coke on the Ni-MgAl, NiCo-MgAl, and Ni-MgAl@CeO₂ is primarily graphitic and inactive, whereas coke on the core-shell Ni-MgAl@CeO₂ and NiCo-MgAl@CeO₂ catalysts consist of both inactive graphitic coke and relatively more active disordered or amorphous coke, with the amorphous form of coke forming approximately 60% of the total. Raman spectra of the spent catalysts under a 638 nm laser (Fig. 6b) support this observation. The first order Raman response from carbon in the range of 1100 – 1700 cm⁻¹ can be deconvoluted into a G band representing the in-plane graphitic lattice of E_{2g} symmetry and D₁, D₂, D₃, and D₄ bands representing the disordered graphitic lattice of various symmetries (Table S3) [52]. The Raman spectra of all the spent catalysts show prominent D and G peaks. The prominent D band is characteristic of multiwalled carbon nanotubes and reflects structural disorder because of the non-planar packaging of the multilayers [53]. The ratio of intensities of the D₁ and G bands (I_{D1}/I_G) is calculated from the deconvolution of spectra to be 2.65 – 2.69 for coke on Ni-MgAl and NiCo-MgAl, and 3.04 – 3.06 for coke on Ni-MgAl@CeO₂ and NiCo-MgAl@CeO₂ (Table S3), indicating a higher degree of disorder in the coke on the core-shell catalysts. Consistent with the TGA and Raman data, the characteristic diffraction peak of graphitic carbon at $2\theta = 26.6^\circ$ is observed in the XRD patterns of the spent Ni-MgAl and NiCo-MgAl catalysts (Fig. S11) but is not discernible in the XRD of the used core-shell Ni-MgAl@CeO₂ and NiCo-MgAl@CeO₂, suggesting low amount of coke and/or low crystallinity. The higher fraction of disordered or amorphous coke compared to inactive graphitic coke on the core-shell catalysts can be attributed to the effect of CeO₂ in the vicinity of Ni surface (further discussion in Section 3.2.4).

It is noted that the temperature of coke oxidation during TG/DTA is lower on the catalysts containing NiCo compared to corresponding catalysts with only Ni. Changes in the nature of coke because of addition of Co in the catalyst are not clearly observed from HRTEM or Raman spectroscopy. It is possible that the higher oxophilicity of NiCo compared to Ni [54] leads to oxidation of coke at lower temperatures on NiCo containing catalysts during the TG-DTA experiment.

In summary, the spent catalyst characterization demonstrates that the addition of the CeO₂ shell to Ni-MgAl or NiCo-MgAl catalysts suppresses the rate of coke deposition during DRM and results in formation of coke that is more disordered or amorphous.

3.2.3. In situ DRIFTS for DRM on core-shell catalyst

An *in situ* DRIFTS experiment was conducted on the core-shell Ni-MgAl@CeO₂ catalyst to gain insights into the mechanistic role of the CeO₂ shell in eliminating coke. In this experiment, the reduced Ni-MgAl@CeO₂ core-shell catalyst was exposed to alternating pulses of CH₄ and CO₂ at the reaction temperature of 600 °C.

DRIFTS spectra of Ni-MgAl@CeO₂ (Fig. 7) during the first methane pulse show ν_{CO} bands of gas-phase CO (2170 and 2110 cm⁻¹) and CO₂ (2360 and 2340 cm⁻¹). The IR bands for CO appear concurrently with that of CH₄ in the transient spectra when the pulse of methane is introduced, and their intensities subsequently decrease with time as methane is purged out of the cell – this indicates that CO is formed as a product. The formation of CO from methane (without any oxidant in the feed) on Ni-MgAl@CeO₂ gives evidence of the participation of oxygen-containing moieties in the catalyst in oxidation of carbonaceous intermediates from methane dissociation. The source of the reactive oxygen moiety in the catalyst can be reasonably inferred to be CeO₂ because it is the only component in the catalyst with redox properties. A comparison of the O₂-TPD profiles of Ni-MgAl and Ni-MgAl@CeO₂

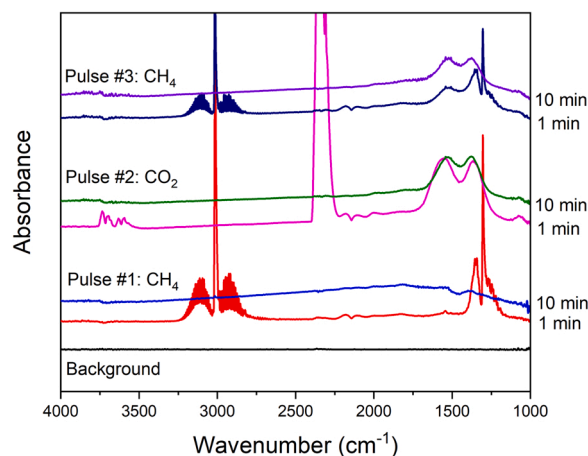


Fig. 7. In situ DRIFTS spectra during alternate pulses of CH₄ and CO₂ at 600 °C with time on Ni-MgAl@CeO₂. Pulses are introduced in the sequence CH₄ → CO₂ → CH₄ after in situ reduction and He purge.

(Fig. 3c) strongly supports this inference because it clearly shows that the addition of CeO₂ imparts oxygen release capacity to the material. We infer that reactive lattice oxygen released from CeO₂ in Ni-MgAl@CeO₂ reacts with carbonaceous intermediates (from methane dissociation) at the interface of Ni and CeO₂ to produce CO/CO₂. This result is significant because it gives evidence of the active role of the CeO₂ shell in oxidizing and removing coke precursors in the Ni-MgAl@CeO₂ core-shell catalyst. These results agree with our previous observations on CeO₂-containing core-shell catalysts [27,28] and is consistent with a bifunctional Mars-van Krevelen type redox mechanism of DRM reported in literature on redox catalysts [5,55].

A subsequent pulse of CO₂ after purging out the methane from the first pulse resulted in the formation of more CO product from the dissociation of CO₂ on the metal surface or on oxygen vacancies created in CeO₂ and the oxidation of residual carbonaceous intermediates, if any, from the first CH₄ pulse. IR bands of surface carbonates (ν_{CO} bands at 1550–1340 cm⁻¹) on the MgAl mixed oxide are also observed, which is consistent with the basic property of the support. A third pulse of CH₄ was introduced after flushing the CO₂ out of the cell. The formation of CO is again observed, indicating that reactive oxygen species in the catalyst are regenerable by CO₂. It is also observed that the intensity of surface carbonate peaks decreases when methane is introduced. This could indicate that surface carbonates on magnesium oxide in the support also take part in oxidation of coke precursors.

3.2.4. Discussion on enhanced coke resistance of core-shell catalysts

A central result from the *in situ* DRIFTS experiment on the core-shell Ni-MgAl@CeO₂ catalyst is the evidence of involvement of oxygen from the CeO₂ shell in the oxidation and removal of carbonaceous intermediates. The high reactivity of CeO₂ lattice oxygen and its participation in gasification of nascent carbon is one of the primary reasons of the enhanced coke resistance of the core-shell catalysts. The participation of CeO₂ in carbon oxidation is expected to happen by a Mars-van Krevelen type redox mechanism [7,28,56], wherein the reaction of carbonaceous intermediates with oxygen from CeO₂ creates oxygen vacancies, that are then cyclically filled up by O from CO₂ dissociation.

We emphasize that interaction/ interface of the metal (Ni or NiCo) with CeO₂ is important for the occurrence of this dual-site redox mechanism of coke oxidation involving CeO₂. The sandwiched structure of the core-shell catalysts with the surface of Ni/MgAl oxide nanosheets covered by porous CeO₂ is expected to maximize this interaction and facilitate this route of coke oxidation. A comparison of the stability of the core-shell Ni-MgAl@CeO₂ with that of the Ni-MgAlCe, which has similar composition but minimal interaction between CeO₂ and Ni, underlines the significance of the core-shell morphology in suppressing coke.

The reactivity of the CeO₂ shell is also the likely reason for the change in nature of coke to more amorphous on the core-shell catalysts. The mechanism of coke formation in DRM is complex and not completely understood, but it is generally accepted that it involves a progressive conversion of amorphous (reactive) carbon to less reactive carbonaceous species by dehydrogenation, polymerization, and rearrangement, and finally to inactive coke with high degrees of graphitization [51]. The enhanced gasification of reactive carbons by the lattice oxygen of CeO₂ may be responsible for mitigating the transformation and graphitization of amorphous carbon into less-active coke. Such an effect of CeO₂ in changing the nature of coke has been reported before [51,57].

The detachment of Ni nanoparticles from the support by tip-growth of carbon nanotubes is another factor that is intricately linked with metal sintering and formation of coke in DRM [9]. Once the active metal nanoparticles are detached, they lose their interaction with the support, thereby losing any functionality of the support in CO₂ activation or coke oxidation. Detached metal nanoparticles are also more prone to sintering, that can, in turn, cause more coking [3,58]. Core-shell structures with thermally stable shells physically hinder metal nanoparticle

detachment from the support [26,59].

The basic sites of MgO in the core is also expected to play a role in coke removal on these catalysts. Basic sites on MgO surface have been reported to form active surface carbonates by adsorbing CO₂, which can react with carbonaceous species to form CO [60]. *In situ* DRIFTS spectra on Ni-MgAl@CeO₂ confirms that surface carbonates are formed when CO₂ is introduced and the intensity of the carbonate peaks decrease upon subsequent introduction of methane, suggesting that the carbonates may be active intermediates. It is likely that both CeO₂ and MgO play a role in carbon oxidation, although it is difficult to deconvolute their individual contributions. The Ni-MgAl or NiCo-MgAl catalysts are characterized by poor coke resistance, which may indicate that the contribution of the basic sites on MgO in coke elimination is minor compared to that of lattice oxygen of CeO₂. The detachment of Ni nanoparticles from the MgAl oxide support in Ni-MgAl or NiCo-MgAl by carbon nanotubes may also prevent any promotional effect of MgO in coke elimination on these non-core-shell catalysts.

In summary, we can attribute the enhanced coke resistance of the CeO₂ coated core-shell catalysts to - a. oxidation of coke precursors by highly reactive lattice oxygen from CeO₂ neighbouring Ni and NiCo nanoparticles, b. the steric effect of the CeO₂ shell, that suppresses metal sintering and the detachment of Ni or NiCo nanoparticles from the support by carbon nanotubes.

3.2.5. Catalyst regenerability

The possibility and methods of regeneration of the core-shell catalyst after long term DRM testing was evaluated. The Ni-MgAl@CeO₂ catalyst was chosen for the regeneration study since it is observed to undergo slight deactivation over the 165-h DRM activity test. It is observed that the core-shell catalyst can be regenerated onstream by stopping the reaction feed and treating the catalyst in a flow of H₂ or CO₂ for 1 h. Details of the regeneration study are provided in the [Supporting Information](#) (Fig. S12). Analysis of the gas product during regeneration in H₂ flow (Fig. S13) shows the formation of methane – we infer that regeneration of the catalyst surface happens by the hydrogenation of amorphous/ reactive carbon, which constitutes a big fraction of coke on the core-shell catalyst, to form methane [61]. The regeneration process is easy to implement, can be done onstream without unloading the catalyst and without any additional cooling/heating, and does not have any induction time for the catalyst to regain activity post treatment.

3.3. Evaluation of catalyst tolerance to poisoning by H₂S

3.3.1. Catalyst performance and stability

The performance of the catalysts in DRM in the presence of H₂S was subsequently studied. DRM was conducted at 800 °C in the presence of 20 ppm H₂S to observe the deactivation characteristics, steady state catalytic activity in the presence of H₂S, and the recovery of activity after stopping H₂S in feed. All the catalysts show close to 93% CH₄ initial conversion in the absence of H₂S in feed (Fig. 8). Upon exposure to H₂S, the Ni-MgAl catalyst started deactivating almost instantaneously and lost approximately 80% of the initial CH₄ conversion activity within 1.5 h in the presence of H₂S. This fast deactivation in the presence of H₂S is in agreement with previous literature on sulfur sensitivity of Ni catalysts in DRM [10,13,18,20] and has been attributed to the strong chemisorption of sulfur on the active Ni sites [20].

CH₄ and CO₂ conversion on the deactivated Ni-MgAl catalyst remained stable at 18% and 32%, respectively. The H₂/CO ratio is observed to drastically drop in the presence of H₂S, with the CO₂ conversion being much higher than CH₄ conversion on the sulfur poisoned catalyst. This suggests that sulfur affects the active sites for the various elementary steps differently, wherein dry reforming sites are poisoned but sites for RWGS are not as significantly affected. Similar observations were reported by Mancino et al. [11] on Rh/ γ -Al₂O₃ and Pawar et al. [17] on Ni/ γ -Al₂O₃ catalysts, where H₂S severely poisoned DRM activity but not RWGS activity, thereby driving down the H₂/CO ratio. It is also

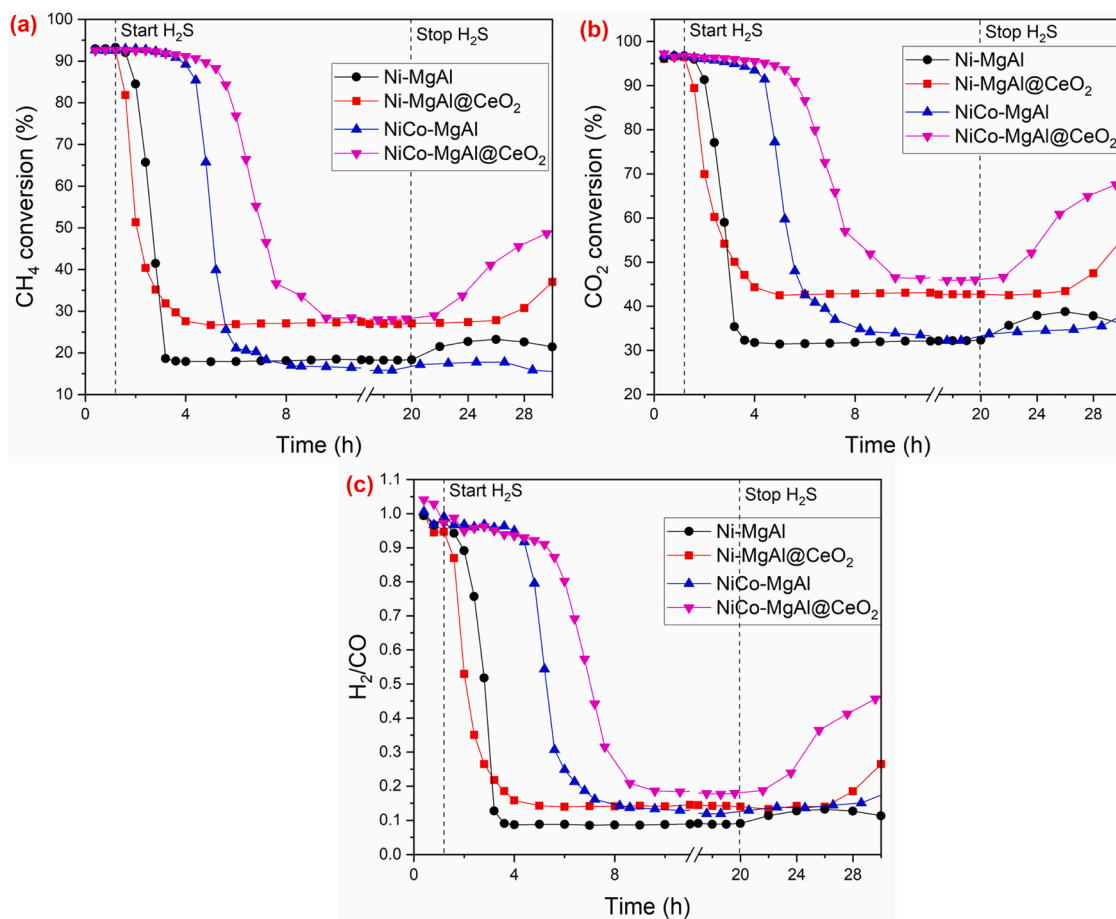


Fig. 8. Catalyst performance in DRM in the presence of H₂S. Reaction conditions: Temperature = 800 °C, pressure = 1 bar, WHSV = 54 Lg⁻¹h⁻¹, CH₄/CO₂/He = 1:1:2.5, H₂S = 20 ppm. WHSV is calculated based on the mixed metal oxide (Ni/CoMgAl) weight.

observed that during DRM in the presence of H₂S, the carbon balance between reactants converted and CO produced is slightly lower than 90% (Fig. S14), indicating that some of the carbon gets converted to coke or other carbonaceous compounds that are not detected by the GC. H₂S flow was discontinued after 18 h and the reaction was continued further with H₂S free feed for 10 h. The catalytic activity of the Ni-MgAl catalyst was not observed to recover significantly after stopping H₂S in the time duration tested, indicating that sulfur is strongly chemisorbed on Ni sites and is not desorbed simply by stopping H₂S in the feed. Methane conversion increased marginally from c.a. 18–23% over 7 h onstream upon stopping H₂S, which is possibly a result of desorption/hydrogenation of sulfur from a small fraction of Ni surface sites (that are characterized by weaker sulfur chemisorption). Beyond that, the activity starts to decline again, which could be an effect of coke formation or metal sintering over time.

Compared to Ni-MgAl, the NiCo-MgAl catalyst showed much better resistance to the initial deactivation in H₂S. Negligible deactivation was observed for 4 h after the introduction of H₂S, with the CH₄ conversion remaining > 90%. The initial delay in deactivation of NiCo-MgAl is a significant advantage from an operational aspect because it allows time to take care of process upsets in upstream units in case of an accidental H₂S increase in the feed, without deactivating the catalyst or affecting downstream units. After the initial stable performance for 4 h, a rapid drop in reactant conversion was observed and the steady state CH₄ conversion in the presence of H₂S after catalyst deactivation was observed to be 17%, similar to that of Ni-MgAl. After stopping H₂S in the feed, the activity was not observed to increase significantly in 10 h onstream time. Conversion on the deactivated NiCo-MgAl after stopping H₂S was even lower than that of Ni-MgAl under similar conditions,

which is possibly a result of higher accumulation of coke on NiCo-MgAl because it was active for methane reforming for a longer duration than Ni-MgAl in the H₂S containing feed.

The Ni-MgAl@CeO₂ core-shell catalyst also deactivated rapidly upon exposure to H₂S, exhibiting a similar behaviour as that of Ni-MgAl, but the steady state activity after deactivation was observed to be higher. The CH₄ and CO₂ conversion remained stable at 28% and 42% during H₂S flow. When H₂S in feed was stopped, the activity of the catalyst was observed to start recovering slowly after approximately 5 h of DRM without H₂S, in contrast to the behaviour of Ni-MgAl.

The NiCo-MgAl@CeO₂ catalyst showed the highest resistance to H₂S deactivation. For the first 5 h of H₂S introduction, the catalyst activity remained stable with > 90% CH₄ conversion. After 8 h in 20 ppm H₂S, the CH₄ and CO₂ conversion dropped to the steady state values of 30% and 46% respectively. The activity was observed to start recovering almost immediately after cessation of H₂S in the feed, showing that the deactivation of NiCo-MgAl@CeO₂ by H₂S is not permanent under these operating conditions.

3.3.2. Characterization of deactivated catalyst after DRM with H₂S in feed

The spent catalysts after 24 h DRM with 20 ppm H₂S in the feed were characterized by TEM-EDX, XRD, XPS, and TPO.

Elemental mapping by TEM-EDX shows the presence of sulfur in various quantities in all the used catalysts after DRM with H₂S-containing feed (Fig. 9, S15, S16). This provides evidence of the adsorption of sulfur on the catalyst surface during the reaction. The amount of sulfur in the spent Ni-MgAl and NiCo-MgAl samples after 24 h reaction was measured by TEM-EDX to be approximately 56% and 27%, respectively, of the total metal atoms (nickel + cobalt) in the catalysts

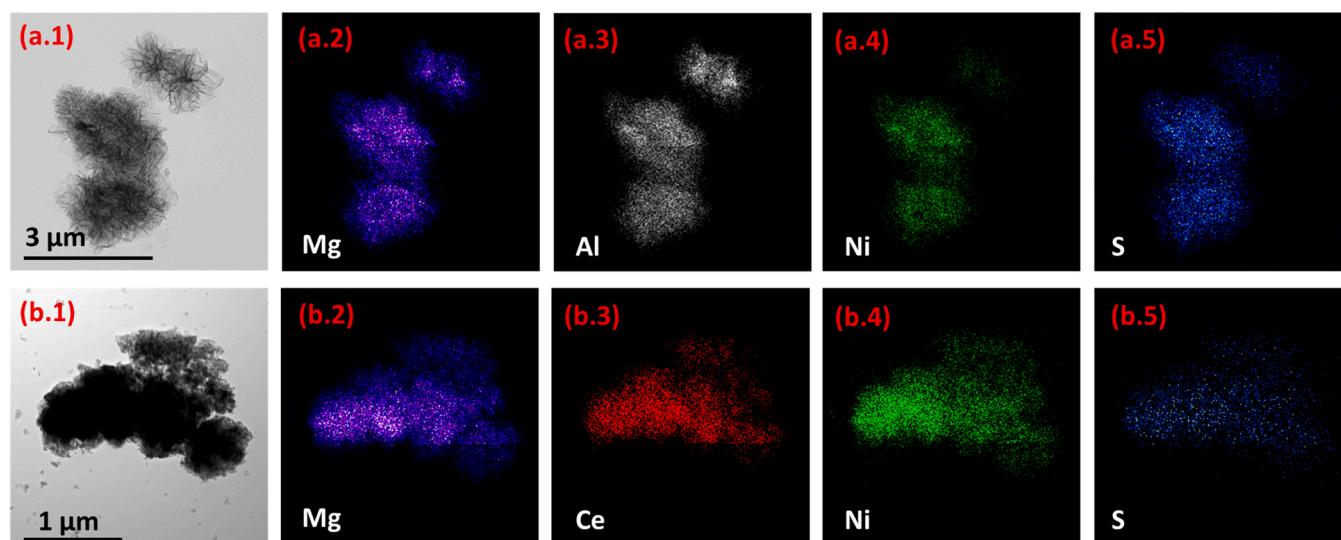


Fig. 9. TEM image and EDX mapping of Mg, Al, Ni, Ce, and S in: (a.1 – a.5) spent Ni-MgAl, and (b.1-b.5) spent Ni-MgAl@CeO₂ after 24 h DRM with 20 ppm H₂S in feed. Reaction conditions: Temperature = 800 °C, pressure = 1 bar, CH₄/CO₂/He = 1:1:2.5, H₂S = 20 ppm.

Table 2

EDX measurement of sulfur content in deactivated catalysts after 24 h reaction with 20 ppm H₂S in feed.

Sample	Sulfur / (Nickel + Cobalt), atom %
Ni-MgAl	56 ± 1.6
NiCo-MgAl	27 ± 2.2
Ni-MgAl@CeO ₂	9 ± 1.5
NiCo-MgAl@CeO ₂	Below detection limit

(Table 2). In comparison, the sulfur content is much lower in the spent core-shell Ni-MgAl@CeO₂ (9% of the Ni atom content) and NiCo-MgAl@CeO₂ (below the detection limit of TEM-EDX).

XRD of the deactivated catalysts (Fig. S17) do not show clear evidence of the formation of nickel or cobalt sulfide phases – which could be because bulk metal sulfides are not present or are poorly crystalline or too low in quantity to be detected by XRD. Thermodynamic analyses reported in literature indicate that bulk nickel sulfides do not form at the temperature and $P_{\text{H}_2\text{S}}/P_{\text{H}_2}$ in the DRM reaction mixture, and surface adsorbed sulfur is expected at the used conditions [62,63]. We recognize that weak peaks of nickel sulfide would be difficult to identify because of overlap with the diffraction patterns of the metal oxide supports (i.e. MgO periclase and MgAl₂O₄ spinel phases) [39].

Ni 2p XPS of the reduced and post-catalytic (deactivated) Ni-MgAl and NiCo-MgAl samples (Fig. S18a) show a prominent change in the binding energy of the Ni 2p_{3/2} peak from c.a. 852.2 eV (characteristic of Ni⁰) and 855.5 eV (characteristic of NiO) in the reduced sample to 857.3 eV in the post-catalytic sample, which is characteristic of NiSO₄ [64]. This peak is attributed to surface nickel sulfide (or sulfur chemisorbed on Ni surface) in the deactivated catalyst (surface nickel sulfide has been reported to readily convert to sulfates when exposed to air during sample handling for XPS measurements). Similarly, the main peak in the Co 2p XPS spectrum of the post-catalytic NiCo-MgAl (Fig. S18b) is shifted to 782.8 eV (characteristic of CoSO₄). We conclude from these results that sulfur is chemisorbed on the surface of both Ni and Co during the reaction. The Ni 2p and Co 2p XPS spectra of the spent core-shell catalysts are non-informative because of poor signal to noise ratio.

Temperature programmed oxidation (TPO) experiments were subsequently conducted on the deactivated catalysts after H₂S-DRM to find the temperature at which the deposited sulfur can be removed by oxidation (Fig. 10). The TPO profile of spent Ni-MgAl shows a distinct

peak for SO₂ (m/z = 48 and 64) at 910 °C. This peak is lower in intensity and shifted to a lower temperature of 850 °C in the TPO profile of NiCo-MgAl. For the core-shell Ni-MgAl@CeO₂, the SO₂ peak is barely discernible (consistent with the lower sulfur content measured by TEM-EDX) and appears at a much lower temperature of 760 °C. Presence of SO₂ in the product during TPO of spent NiCo-MgAl@CeO₂ could not be clearly identified, presumably because of low sulfur content in the sample. A central result from the spent catalyst characterization by TPO is that sulfur can be oxidatively removed from the core-shell CeO₂ containing catalysts at significantly lower temperature than from the catalysts without CeO₂.

3.3.3. Evidence of H₂S oxidation by CO₂ in core-shell catalysts

Characterization of the spent catalysts after DRM with H₂S by TPO (as discussed in Section 3.3.2) provides evidence of the oxidative removal of sulfur deposits by O₂ at lower temperatures for the CeO₂ containing core-shell catalysts than the catalysts without the CeO₂ shell. The catalyst performance during DRM with H₂S-containing feed and the quantification of sulfur deposits on the spent catalysts suggest that CeO₂ in the core-shell catalysts may be involved in catalysing oxidative removal of H₂S during the reaction. To examine the possibility of H₂S oxidation by CO₂ during the DRM reaction at 800 °C on the CeO₂ containing core-shell catalysts, the NiMgAl@CeO₂ catalyst was exposed to H₂S and CO₂ gases, while monitoring the product gas by mass spectrometry (Fig. 11). When the reduced NiMgAl@CeO₂ was exposed to H₂S (300 ppm, balance He), traces of SO₂ (monitored by mass spectrometer at m/z = 48 and 64) were observed in the product gas, indicating slow oxidation of H₂S by the lattice oxygen of CeO₂. When the gas flow was switched to CO₂ (10%, balance He), similar levels of SO₂ was observed in the product, suggesting the slow oxidative removal of adsorbed sulfur from the catalyst by CO₂. The concentration of SO₂ in the product was observed to drastically increase when both CO₂ and H₂S (10% CO₂, 300 ppm H₂S, balance He) were introduced into the reactor. The results clearly show that at the used reaction temperature, CO₂ can react with H₂S to produce SO₂ on the NiMgAl@CeO₂ catalyst. Formation of SO₂ is also observed when pure CeO₂ is exposed to a mixture of CO₂ and H₂S at 800 °C in a control experiment, confirming the role of CeO₂ in H₂S oxidation (Fig. S19). The continuous oxidation of H₂S by CO₂ catalysed by CeO₂ during DRM can suppress the chemisorption of sulfur on the Ni surface in the core-shell catalyst and may be responsible for the higher steady state activity of the core-shell catalysts during DRM in the presence of H₂S in the feed.

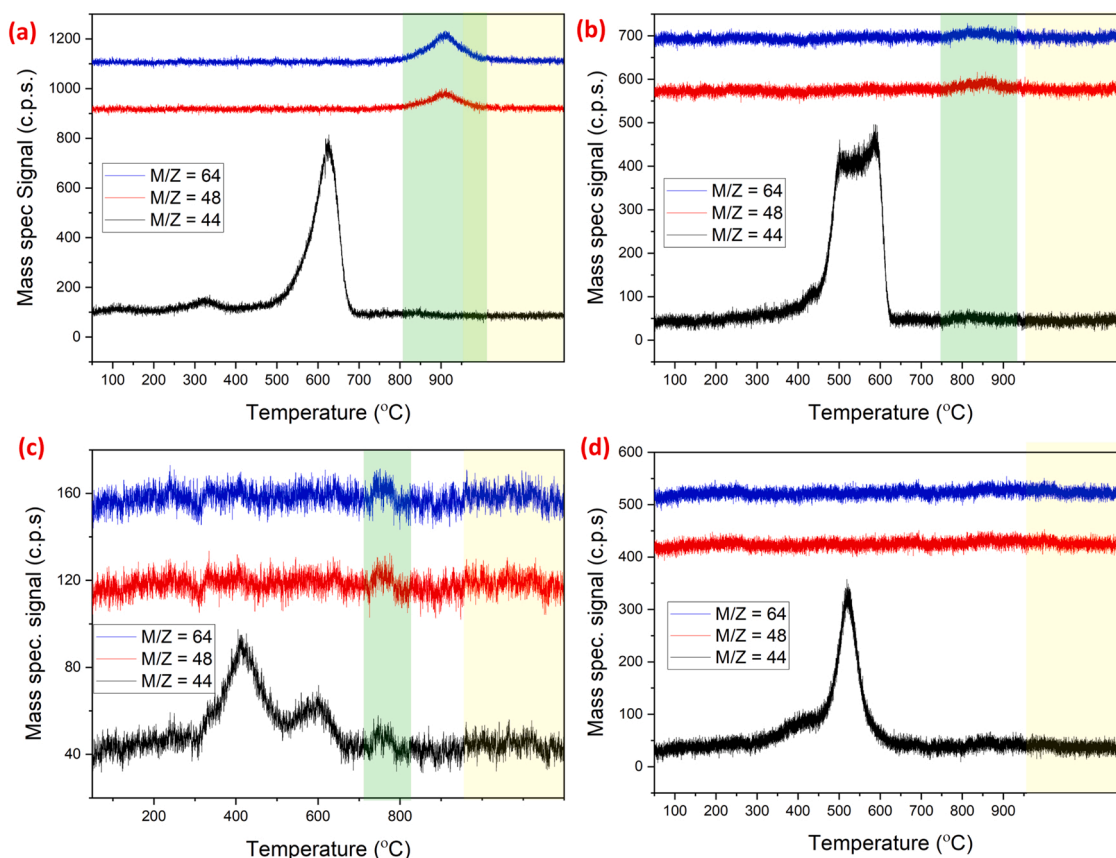


Fig. 10. Mass spectrometric analysis of product gas during TPO of spent catalysts after 24 h DRM with 20 ppm H₂S in feed.

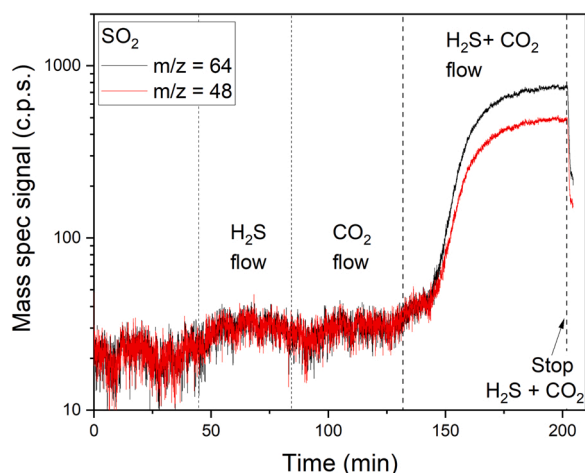


Fig. 11. Mass spectrometry of outlet gas during flow of CO₂ and H₂S on Ni-MgAl@CeO₂ at 800 °C. Ni-MgAl@CeO₂ was treated in H₂ for 1 h at 800 °C, followed by purging the reactor with He. H₂S (300 ppm, balance He), CO₂ (10%, balance He), and a mixture of CO₂ and H₂S (10% CO₂, 300 ppm H₂S, balance He) was introduced sequentially into the reactor held at 800 °C. Continuous analysis of the product by a mass spectrometer shows the formation of SO₂ ($m/z = 48, 64$) with time.

3.3.4. Discussion on enhanced sulfur tolerance of core-shell catalysts

The rapid deactivation of Ni-MgAl in the H₂S containing DRM feed is attributed primarily to the chemisorption of sulfur on nickel, which is evident from the XPS characterization of the spent catalyst (under DRM conditions, these surface sulfides are subsequently transformed into the thermodynamically more stable sulfates that are observed by XPS). H₂S

has been reported to readily decompose with very low energy barriers on nickel surface to form atomic sulfur and hydrogen [65]. The adsorption energy of H₂S and the dissociated atomic sulfur on a nickel surface has been predicted by theoretical calculations [65,66] to be significantly higher than that of the reactants in DRM, resulting in blockage of active catalytic sites by sulfur chemisorption. The Ni-MgAl catalyst deactivated by 80% of its initial activity at a contacting time at which the molar amounts of H₂S passed over the catalysts was approximately 82% of the moles of surface nickel in the catalyst (Table S4). This almost stoichiometric correlation between catalyst deactivation and sulfur atoms in the feed strongly supports the inference that titration and blocking of surface nickel sites by sulfur results in loss of DRM activity.

The addition of cobalt in NiCo-MgAl delays the onset of deactivation by H₂S compared to Ni-MgAl. Similar delay in deactivation is observed for NiCo-MgAl@CeO₂ compared to Ni-MgAl@CeO₂, indicating that this initial resistance to deactivation can be attributed to the presence of cobalt. Our observations agree with previous experimental reports on the promoting effect of cobalt on nickel catalysts in sulfur tolerance [24, 25,67]. The reason behind the promoting role of Co on sulfur tolerance is not clearly established, but can likely be attributed to an electronic interaction exerted by Co on Ni [67]. On its own, cobalt metal has a slightly lower affinity for sulfur as compared to nickel [68]. Contradictory reports exist for sulfur chemisorption on NiCo alloys compared to unalloyed Ni. Lower equilibrium sulfur coverage was experimentally observed on an alumina supported NiCo alloy compared to alumina supported Ni nanoparticles during isothermal H₂S chemisorption experiments [69]. However, reported DFT studies have indicated a higher energy of adsorption of H₂S and atomic sulfur on NiCo alloy surface relative to unalloyed nickel, indicating lower sulfur tolerance of the alloy [62,70]. Although it is possible that the cobalt atoms in NiCo-MgAl preferentially adsorb sulfur, leaving the nickel surface free and available

for catalysis for a longer time and thereby delaying catalyst deactivation, the total H₂S passed over the catalyst in the duration required for NiCo-MgAl to deactivate by 80% of its initial activity corresponds to approximately 302% of the nickel content or 153% of the total nickel and cobalt content in the catalyst (Table S4). These values are higher than that for Ni-MgAl and suggests a less than stoichiometric correlation between sulfur atoms in the feed and sulfur chemisorbed on Ni/Co surface, in agreement with EDX characterization of the spent catalyst showing a lower total sulfur content on NiCo-MgAl than on Ni-MgAl. These results indicate that the addition of cobalt lowers the overall rate of sulfur adsorption in the catalyst, and that the role of cobalt is more than merely as a sacrificial element.

Although Co initially exists as a fully-reduced NiCo alloy in the fresh (reduced) catalyst, it is sufficiently oxophilic to be partially oxidized into Co(II) oxide clusters under DRM conditions [67]. In the partially de-alloyed system, these oxide clusters can alter the kinetics of H₂S chemisorption on neighbouring metal nanoparticles via an electronic effect, thereby explaining the enhanced breakthrough time. The observation of CoSO₄ in the spent catalyst by XPS can be attributed to the reaction between the Co(II) oxide clusters and sulfur chemisorbed to the metal-oxide interface. Product analysis during temperature programmed oxidation of the spent catalysts shows a lower temperature of sulfur oxidation on NiCo-MgAl compared to Ni-MgAl, consistent with weaker sulfur chemisorption on NiCo compared to Ni accompanied by an autocatalytic effect caused by oxophilic CoO_x facilitating oxygen activation and the removal of sulfur from Ni.

With continuous exposure to H₂S in the feed, the activities of all the catalysts ultimately decline after different lengths of delay to reach a stable steady state activity. Compared to Ni-MgAl and NiCo-MgAl, both the core-shell catalysts with CeO₂ coating show a much higher steady state catalytic activity (approximately 1.7 – 1.9 times higher CH₄ conversion) in the presence of H₂S. Consistently, the EDX mapping indicates a decrease in sulfur content by more than 5 times in the spent core-shell catalysts after 24 h reaction compared to the CeO₂-free catalysts. We see evidence of the formation of SO₂ by mass spectrometry when H₂S and CO₂ are co-fed on the CeO₂ containing core-shell catalysts. We hence hypothesize that the higher activity of the core-shell catalysts in the presence of H₂S and the lower sulfur deposition on the catalysts is a result of the catalytic effect of the CeO₂ shell in oxidizing and removing H₂S and suppressing its chemisorption on nickel sites. This inference is also supported by the TPO profiles of the deactivated catalysts that shows that sulfur deposits on Ni-MgAl@CeO₂ can be oxidatively removed by air at much lower temperatures (c.a. 760 °C) than those on Ni-MgAl (c.a. 910 °C), evidencing the role of CeO₂ in facilitating sulfur oxidation and removal.

These results are consistent with reported experimental studies on pure CeO₂ materials (without added metals) [71] that have shown that lattice oxygen released from CeO₂ can oxidize H₂S at elevated temperatures to form SO₂, sulfates/ sulfites, or sulfur atoms on the surface of or substituted in the lattice of CeO₂. The oxidation of H₂S by CeO₂ creates oxygen vacancies, which can be replenished by CO₂ in the reaction atmosphere [71]. The stability of sulfates/ sulfites on the surface of CeO₂ depends on temperature and H₂S/ SO₂ partial pressure, and cerium sulfate has been reported to completely decompose at temperatures between 600 and 800 °C to form the oxide and SO₂ [72]. Thus, during DRM reaction at 800 °C, CeO₂ in the core-shell catalysts is inferred to catalyse the oxidation and removal of H₂S or its dissociation products as sulfur oxide, thereby decreasing the coverage of sulfur on nickel and imparting higher steady state activity to the core-shell catalysts in H₂S containing feed than the catalysts without the CeO₂ shell. Electronic modifications to nickel by its interaction with CeO₂, akin to that proposed above for the role of cobalt, could also affect its affinity to chemisorb sulfur, but such effects cannot be discerned from our experimental observations.

Although H₂S can also directly chemisorb on CeO₂ surfaces, particularly in the presence of oxygen defects [73], this interaction is typically

weaker than that over Ni surfaces [62] and thus less likely to play an important role in our catalysts. Indeed, as the addition of CeO₂ shell to Ni-MgAl did not significantly alter the onset time of deactivation (Fig. 8a), CeO₂ does not appear to play the role of a sacrificial sulfur trap, as proposed by Ocsachoque et al. for ceria-supported Ni catalysts [18], in our materials. This difference may be due to the high density of metal-oxide interfacial sites engendered by the core-shell architecture [27], which strongly promotes the movement of lattice oxygen from CeO₂ to the Ni surface that enables the chemisorbed sulfur to be easily oxidized.

3.3.5. Regeneration of activity after stopping H₂S

DRM activity of the core-shell catalysts start increasing once H₂S in the feed is stopped. The supply of lattice oxygen from the CeO₂ shell is proposed to be responsible for the gradual recovery of catalytic activity after stopping H₂S in feed by aiding in the oxidation and removal of the adsorbed sulfur. A longer catalytic test showed that > 75% of the initial methane conversion activity of NiCo-MgAl@CeO₂ can be recovered in 45 h onstream after H₂S feed is stopped (Fig. S20).

In summary, the core-shell NiCo-MgAl@CeO₂ catalyst shows significantly enhanced tolerance to H₂S poison in the feed in terms of the initial delay in deactivation, steady state activity in the presence of H₂S and recovery of activity after H₂S is stopped. A comparison of DRM performance in the presence of H₂S with previously reported catalysts is presented in Table S5.

4. Conclusion

A bifunctional core-shell structured NiCo-MgAl@CeO₂ catalyst was developed for dry reforming of methane with the aim of increasing resistance to deactivation by coke and H₂S poisoning. The LDH derived NiCo-MgAl core showed excellent catalytic activity for DRM because of the synergistic effect of the NiCo alloy and the acid/base properties of the MgAl mixed oxide support but formed high amounts of coke that led to rapid deactivation. Coating a ceria shell to form the NiCo-MgAl@CeO₂ core-shell catalyst dramatically suppressed coke formation, with the catalyst showing extremely stable DRM performance for 1 week at 600 °C. Characterization of coke in the spent catalysts indicate the CeO₂ shell reduced coke deposition rate by two orders of magnitude and also changed the nature of coke to more reactive amorphous carbon. *In situ* DRIFTS experiment on the core-shell catalyst provides evidence of the participation of lattice oxygen of CeO₂ in oxidation of carbonaceous intermediates.

The sulfur tolerance of the catalysts during DRM was subsequently investigated. The NiCo-MgAl@CeO₂ catalyst demonstrated significantly enhanced resistance to H₂S induced deactivation compared to Ni-MgAl, NiCo-MgAl, and Ni-MgAl@CeO₂, when tested for DRM at 800 °C in the presence of 20 ppm H₂S. The presence of Co in the mixed oxide core of NiCo-MgAl@CeO₂ was observed to delay deactivation upon H₂S exposure, whereas addition of the CeO₂ shell resulted in higher steady state activity in the presence of H₂S and in gradual recovery of activity after H₂S cessation. Spent catalyst characterization showed significantly lower sulfur content in the core-shell catalysts compared to the catalysts without the ceria shell. Mass spectrometric product analysis while co-feeding H₂S and CO₂ shows evidence of SO₂ formation on the CeO₂ containing core-shell catalysts, suggesting that H₂S can be oxidatively removed by CO₂ in the presence of CeO₂ during the DRM reaction. Consistently, the temperature required to oxidatively remove sulfur from the spent catalysts was significantly lower for the catalysts with the CeO₂ shell. The enhanced sulfur resistance of the core-shell catalyst is, hence, attributed to the involvement of reactive lattice oxygen of CeO₂ in activating CO₂ and catalysing the oxidation and removal of sulfur, thereby suppressing the poisoning of active sites. Recovery of catalytic activity of the core-shell NiCo-MgAl@CeO₂ upon stopping H₂S may also be attributed to the oxidative removal of chemisorbed sulfur facilitated by the reactive lattice oxygen of CeO₂.

The combination of the NiCo-MgAl mixed oxide core and the CeO₂ shell in NiCo-MgAl@CeO₂, thus, helps in simultaneously achieving excellent coke resistance in DRM and enhanced tolerance to H₂S contaminants in the feed. Thus, this work shows how a systematic and rational combination of catalytic materials with complementary properties in a bifunctional core-shell structure can help in suppressing catalyst deactivation in dry reforming of methane or biogas by both coke and sulfur poisoning.

CRedit authorship contribution statement

Sonali Das: Conceptualization, Methodology, Investigation, Validation, Writing – original draft, Visualization. **Kang Hui Lim:** Investigation, Validation, Writing – review & editing, Visualization. **Terry Z. H. Gani:** Investigation. **Saeed Aksari:** Investigation, Validation. **Sibudjing Kawi:** Supervision, Writing – review & editing, Funding acquisition.

Declaration of Competing Interest

The authors declare that they have no known competing financial interests or personal relationships that could have appeared to influence the work reported in this paper.

Data Availability

Data will be made available on request.

Acknowledgement

The research was supported by the FRC MOE T1 Project (WBS: A-0009184-00-00) and A*STAR LCERFI Project (WBS: A-8000278-00-00). The authors also gratefully thank the National University of Singapore for supporting the research.

Appendix A. Supporting information

Supplementary data associated with this article can be found in the online version at doi:10.1016/j.apcatb.2022.122141.

References

- [1] Z. Bian, S. Das, M.H. Wai, P. Hongmanorom, S. Kawi, A review on bimetallic nickel-based catalysts for CO₂ reforming of methane, *ChemPhysChem* 18 (2017) 3117–3134.
- [2] S. Kawi, Y. Kathiraser, J. Ni, U. Oemar, Z. Li, E.T. Saw, Progress in synthesis of highly active and stable nickel-based catalysts for carbon dioxide reforming of methane, *ChemSusChem* 8 (2015) 3556–3575.
- [3] S. Das, A. Jangam, S. Xi, A. Borgna, K. Hidajat, S. Kawi, Highly dispersed ni/silica by carbonization–calcination of a chelated precursor for coke-free dry reforming of methane, *ACS Appl. Energy Mater.* 3 (2020) 7719–7735.
- [4] L.-Y. Shi, Y.-X. Li, D.-M. Xue, P. Tan, Y. Jiang, X.-Q. Liu, L.-B. Sun, Fabrication of highly dispersed nickel in nanoconfined spaces of as-made SBA-15 for dry reforming of methane with carbon dioxide, *Chem. Eng. J.* 390 (2020), 124491.
- [5] S. Das, S. Bhattar, L. Liu, Z. Wang, S. Xi, J.J. Spivey, S. Kawi, Effect of partial Fe substitution in La_{0.9}Sr_{0.1}NiO₃ perovskite-derived catalysts on the reaction mechanism of methane dry reforming, *ACS Catal.* (2020) 12466–12486.
- [6] J. Horlyck, C. Lawrey, E.C. Lovell, R. Amal, J. Scott, Elucidating the impact of Ni and Co loading on the selectivity of bimetallic NiCo catalysts for dry reforming of methane, *Chem. Eng. J.* 352 (2018) 572–580.
- [7] A. Jangam, S. Das, N. Dewangan, P. Hongmanorom, W.M. Hui, S. Kawi, Conversion of CO₂ to C₁ chemicals: catalyst design, kinetics and mechanism aspects of the reactions, *Catal. Today* (2019).
- [8] M. Wang, Q. Zhang, T. Zhang, Y. Wang, J. Wang, K. Long, Z. Song, X. Liu, P. Ning, Facile one-pot synthesis of highly dispersed Ni nanoparticles embedded in HMS for dry reforming of methane, *Chem. Eng. J.* 313 (2017) 1370–1381.
- [9] Z. Li, S. Das, P. Hongmanorom, N. Dewangan, M.H. Wai, S. Kawi, Silica-based micro- and mesoporous catalysts for dry reforming of methane, *Catal. Sci. Technol.* 8 (2018) 2763–2778.
- [10] Y. Gao, J. Jiang, Y. Meng, F. Yan, A. Aihemaiti, A review of recent developments in hydrogen production via biogas dry reforming, *Energy Convers. Manag.* 171 (2018) 133–155.
- [11] G. Mancino, S. Cimino, L. Lisi, Sulphur poisoning of alumina supported Rh catalyst during dry reforming of methane, *Catal. Today* 277 (2016) 126–132.
- [12] S.-A. Theofanis, J.A.Z. Pieterse, H. Poelman, A. Longo, M.K. Sabbe, M. Virginie, C. Detavernier, G.B. Marin, V.V. Galvita, Effect of Rh in Ni-based catalysts on sulfur impurities during methane reforming, *Appl. Catal. B Environ.* 267 (2020), 118691.
- [13] W.S. Jablonski, S.M. Villano, A.M. Dean, A comparison of H₂S, SO₂, and COS poisoning on Ni/YSZ and Ni/K₂O–CaAl₂O₄ during methane steam and dry reforming, *Appl. Catal. A Gen.* 502 (2015) 399–409.
- [14] A. Cavalli, R. Bernardini, T. Del Carlo, P.V. Aravind, Effect of H₂S and HCl on solid oxide fuel cells fed with simulated biosyngas containing primary tar, *Energy Sci. Eng.* 7 (2019) 2456–2468.
- [15] A. Hagen, A. Winiwarter, H. Langnickel, G. Johnson, SOFC operation with real biogas, *Fuel Cells* 17 (2017) 854–861.
- [16] J. Ashok, S. Das, N. Dewangan, S. Kawi, H₂S and NO_x tolerance capability of CeO₂ doped La_{1-x}Ce_xCo_{0.5}Ti_{0.5}O_{3-δ} perovskites for steam reforming of biomass tar model reaction, *Energy Convers. Manag.* X (1) (2019), 100003.
- [17] V. Pawar, S. Appari, D.S. Monder, V.M. Janardhanan, Study of the combined deactivation due to sulfur poisoning and carbon deposition during biogas dry reforming on supported Ni catalyst, *Ind. Eng. Chem. Res.* 56 (2017) 8448–8455.
- [18] M.A. Ocsachoque, J.I. Eugenio Russman, B. Irigoyen, D. Gazzoli, M.G. González, Experimental and theoretical study about sulfur deactivation of Ni/CeO₂ and Rh/CeO₂ catalysts, *Mater. Chem. Phys.* 172 (2016) 69–76.
- [19] C. Xie, Y. Chen, Y. Li, X. Wang, C. Song, Influence of sulfur on the carbon deposition in steam reforming of liquid hydrocarbons over CeO₂–Al₂O₃ supported Ni and Rh catalysts, *Appl. Catal. A Gen.* 394 (2011) 32–40.
- [20] X. Chen, J. Jiang, F. Yan, K. Li, S. Tian, Y. Gao, H. Zhou, Dry reforming of model biogas on a Ni/SiO₂ catalyst: overall performance and mechanisms of sulfur poisoning and regeneration, *ACS Sustain. Chem. Eng.* 5 (2017) 10248–10257.
- [21] J. Blanchard, I. Achouri, N. Abatzoglou, H₂S poisoning of NiAl₂O₄/Al₂O₃–YSZ catalyst during methane dry reforming, *Can. J. Chem. Eng.* 94 (2016) 650–654.
- [22] M. Gaillard, M. Virginie, A.Y. Khodakov, New molybdenum-based catalysts for dry reforming of methane in presence of sulfur: a promising way for biogas valorization, *Catal. Today* 289 (2017) 143–150.
- [23] R. Chein, Z.-W. Yang, H₂S effect on dry reforming of biogas for syngas production, *Int. J. Energy Res.* 43 (2019) 3330–3345.
- [24] B. Saha, A. Khan, H. Ibrahim, R. Idem, Evaluating the performance of non-precious metal based catalysts for sulfur-tolerance during the dry reforming of biogas, *Fuel* 120 (2014) 202–217.
- [25] S.T. Misture, K.M. McDevitt, K.C. Glass, D.D. Edwards, J.Y. Howe, K.D. Rector, H. He, S.C. Vogel, Sulfur-resistant and regenerable Ni/Co spinel-based catalysts for methane dry reforming, *Catal. Sci. Technol.* 5 (2015) 4565–4574.
- [26] S. Das, J. Pérez-Ramírez, J. Gong, N. Dewangan, K. Hidajat, B.C. Gates, S. Kawi, Core-shell structured catalysts for thermocatalytic, photocatalytic, and electrocatalytic conversion of CO₂, *Chem. Soc. Rev.* 49 (2020) 2937–3004.
- [27] S. Das, J. Ashok, Z. Bian, N. Dewangan, M.H. Wai, Y. Du, A. Borgna, K. Hidajat, S. Kawi, Silica–Ceria sandwiched Ni core-shell catalyst for low temperature dry reforming of biogas: coke resistance and mechanistic insights, *Appl. Catal. B Environ.* 230 (2018) 220–236.
- [28] S. Das, A. Jangam, S. Jayaprakash, S. Xi, K. Hidajat, K. Tomishige, S. Kawi, Role of lattice oxygen in methane activation on Ni-Phyllosilicate@Ce_{1-x}Zr_xO₂ core-shell catalyst for methane dry reforming: Zr doping effect, mechanism, and kinetic study, *Appl. Catal. B: Environ.* (2021), 119998.
- [29] N. Dewangan, W.M. Hui, S. Jayaprakash, A.-R. Bawah, A.J. Poojito, T. Jie, A. Jangam, K. Hidajat, S. Kawi, Recent progress on layered double hydroxide (LDH) derived metal-based catalysts for CO₂ conversion to valuable chemicals, *Catal. Today* 356 (2020) 490–513.
- [30] K. Song, M. Lu, S. Xu, C. Chen, Y. Zhan, D. Li, C. Au, L. Jiang, K. Tomishige, Effect of alloy composition on catalytic performance and coke-resistance property of Ni-Cu/Mg(AlO) catalysts for dry reforming of methane, *Appl. Catal. B Environ.* 239 (2018) 324–333.
- [31] R. Dębek, M. Radlik, M. Motak, M.E. Galvez, W. Turek, P. Da Costa, T. Grzybek, Ni-containing Ce-promoted hydrotalcite derived materials as catalysts for methane reforming with carbon dioxide at low temperature – on the effect of basicity, *Catal. Today* 257 (2015) 59–65.
- [32] X. Zhang, Z. Wang, N. Qiao, S. Qu, Z. Hao, Selective catalytic oxidation of H₂S over well-mixed oxides derived from Mg₂Al₂V_{1-x} layered double hydroxides, *ACS Catal.* 4 (2014) 1500–1510.
- [33] Y. Shiratori, M. Sakamoto, T. Uchida, H. Le, T. Quang-Tuyen, K. Sakaki, Hydrotalcite-dispersed paper-structured catalyst for the dry reforming of methane, *Int. J. Hydrog. Energy* 40 (2015) 10807–10815.
- [34] X. Zhong, J. Hu, Y. Zhou, M. He, Y. Wang, Y. Tong, L. Fan, Z. Cai, Q. Ding, Template-free hydrothermal synthesis of 3D flower-like hollow Mg-Al layered double hydroxides microspheres for high-performance optical diffusers, *Mater. Lett.* 211 (2018) 343–347.
- [35] H.-P. Ren, Y.-H. Song, W. Wang, J.-G. Chen, J. Cheng, J. Jiang, Z.-T. Liu, Z.-W. Liu, Z. Hao, J. Lu, Insights into CeO₂-modified Ni–Mg–Al oxides for pressurized carbon dioxide reforming of methane, *Chem. Eng. J.* 259 (2015) 581–593.
- [36] D.Y. Kalai, K. Stangeland, W.M. Tucho, Y. Jin, Z. Yu, Biogas reforming on hydrotalcite-derived Ni-Mg-Al catalysts: the effect of Ni loading and Ce promotion, *J. CO₂ Util.* 33 (2019) 189–200.
- [37] J. Ashok, Y. Kathiraser, M.L. Ang, S. Kawi, Bi-functional hydrotalcite-derived NiO–CaO–Al₂O₃ catalysts for steam reforming of biomass and/or tar model compound at low steam-to-carbon conditions, *Appl. Catal. B Environ.* 172–173 (2015) 116–128.

- [38] W. Liu, S. Xu, R. Liang, M. Wei, D.G. Evans, X. Duan, In situ synthesis of nitrogen-doped carbon dots in the interlayer region of a layered double hydroxide with tunable quantum yield, *J. Mater. Chem. C* 5 (2017) 3536–3541.
- [39] X. Li, Y. Huang, Q. Zhang, C. Luan, V.A. Vinokurov, W. Huang, Highly stable and anti-coking Ni/MoCeZr/MgAl₂O₄-MgO complex support catalysts for CO₂ reforming of CH₄: effect of the calcination temperature, *Energy Convers. Manag.* 179 (2019) 166–177.
- [40] H. Arbag, S. Yasyerli, N. Yasyerli, G. Dogu, T. Dogu, Enhancement of catalytic performance of Ni based mesoporous alumina by Co incorporation in conversion of biogas to synthesis gas, *Appl. Catal. B Environ.* 198 (2016) 254–265.
- [41] D. Li, L. Wang, M. Koike, Y. Nakagawa, K. Tomishige, Steam reforming of tar from pyrolysis of biomass over Ni/Mg/Al catalysts prepared from hydrotalcite-like precursors, *Appl. Catal. B Environ.* 102 (2011) 528–538.
- [42] R. Debek, M. Motak, M.E. Galvez, T. Grzybek, P. Da Costa, Promotion effect of zirconia on Mg(Ni,Al)O mixed oxides derived from hydrotalcites in CO₂ methane reforming, *Appl. Catal. B Environ.* 223 (2018) 36–46.
- [43] R. Debek, M.E. Galvez, F. Launay, M. Motak, T. Grzybek, P. Da Costa, Low temperature dry methane reforming over Ce, Zr and CeZr promoted Ni–Mg–Al hydrotalcite-derived catalysts, *Int. J. Hydrog. Energy* 41 (2016) 11616–11623.
- [44] J.I. Di Cosimo, V.K. Diez, M. Xu, E. Iglesia, C.R. Apesteguía, Structure and Surface and Catalytic Properties of Mg–Al Basic Oxides, *J. Catal.* 178 (1998) 499–510.
- [45] I. Luisetto, S. Tuti, C. Romano, M. Boaro, E. Di Bartolomeo, J.K. Kesavan, S. S. Kumar, K. Selvakumar, Dry reforming of methane over Ni supported on doped CeO₂: new insight on the role of dopants for CO₂ activation, *J. CO₂ Util.* 30 (2019) 63–78.
- [46] B. Nematollahi, M. Rezaei, E.N. Lay, Preparation of highly active and stable NiO–CeO₂ nanocatalysts for CO selective methanation, *Int. J. Hydrog. Energy* 40 (2015) 8539–8547.
- [47] J. Ashok, L. Falbo, S. Das, N. Dewangan, C.G. Visconti, S. Kawi, Catalytic CO₂ conversion to added-value energy rich C1 products, in: M. Aresta, I. Karimi, S. Kawi (Eds.), *An Economy Based on Carbon Dioxide and Water: Potential of Large Scale Carbon Dioxide Utilization*, Springer International Publishing, Cham, 2019, pp. 155–210.
- [48] M.K. Nikoo, N.A.S. Amin, Thermodynamic analysis of carbon dioxide reforming of methane in view of solid carbon formation, *Fuel Processing Technology* (2011) 678–691.
- [49] K.Y. Koo, H.-S. Roh, Y.T. Seo, D.J. Seo, W.L. Yoon, S.B. Park, Coke study on MgO-promoted Ni/Al₂O₃ catalyst in combined H₂O and CO₂ reforming of methane for gas to liquid (GTL) process, *Appl. Catal. A Gen.* 340 (2008) 183–190.
- [50] B.N. Naidu, K.D.P.L. Kumar, H. Saini, M. Kumar, T.N. Kumar, V.V.D.N. Prasad, Coke deposition over Ni-based catalysts for dry reforming of methane: effects of MgO–Al₂O₃ support and ceria, lanthana promoters, *J. Environ. Chem. Eng.* 10 (2022), 106980.
- [51] N. Wang, K. Shen, L. Huang, X. Yu, W. Qian, W. Chu, Facile route for synthesizing ordered mesoporous Ni–Ce–Al oxide materials and their catalytic performance for methane dry reforming to hydrogen and syngas, *ACS Catal.* 3 (2013) 1638–1651.
- [52] A. Sadezky, H. Muckenhuber, H. Grothe, R. Niessner, U. Pöschl, Raman microspectroscopy of soot and related carbonaceous materials: Spectral analysis and structural information, *Carbon* 43 (2005) 1731–1742.
- [53] S.L.H. Rebelo, A. Guedes, M.E. Szeftczyk, A.M. Pereira, J.P. Araújo, C. Freire, Progress in the Raman spectra analysis of covalently functionalized multiwalled carbon nanotubes: unraveling disorder in graphitic materials, *Phys. Chem. Chem. Phys.* 18 (2016) 12784–12796.
- [54] W. Tu, M. Ghoussoub, C.V. Singh, Y.-H.C. Chin, Consequences of surface oxophilicity of Ni, Ni–Co, and Co clusters on methane activation, *J. Am. Chem. Soc.* 139 (2017) 6928–6945.
- [55] M.A. Vasiliades, P. Djinić, L.F. Davlyatova, A. Pintar, A.M. Efstathiou, Origin and reactivity of active and inactive carbon formed during DRM over Ni/Ce_{0.38}Zr_{0.62}O_{2-δ} studied by transient isotopic techniques, *Catal. Today* 299 (2018) 201–211.
- [56] J. Toyir, P. Gelin, H. Belatel, A. Kaddouri, Ir/Ce_{0.9}Gd_{0.1}O_{2-x} as a new potential anode component in solid oxide fuel cells integrating the concept of gradual internal reforming of methane, *Catal. Today* 157 (2010) 451–455.
- [57] R. Patel, A.S. Al-Fatesh, A.H. Fakeeha, Y. Arafat, S.O. Kasim, A.A. Ibrahim, S.A. Al-Zahrani, A.E. Abasaed, V.K. Srivastava, R. Kumar, Impact of ceria over WO₃–ZrO₂ supported Ni catalyst towards hydrogen production through dry reforming of methane, *Int. J. Hydrog. Energy* 46 (2021) 25015–25028.
- [58] J.-H. Kim, D.J. Suh, T.-J. Park, K.-L. Kim, Effect of metal particle size on coking during CO₂ reforming of CH₄ over Ni–alumina aerogel catalysts, *Appl. Catal. A: Gen.* 197 (2000) 191–200.
- [59] S. Das, S. Kawi, Core-shell structured catalysts for catalytic conversion of CO₂ to syngas, in: H. Yamashita, H. Li (Eds.), *Core-Shell and Yolk-Shell Nanocatalysts*, Springer, Singapore, Singapore, 2021, pp. 121–149.
- [60] S. Jiang, Y. Lu, S. Wang, Y. Zhao, X. Ma, Insight into the reaction mechanism of CO₂ activation for CH₄ reforming over NiO–MgO: a combination of DRIFTS and DFT study, *Appl. Surf. Sci.* 416 (2017) 59–68.
- [61] K. Nikooyeh, R. Clemmer, V. Alzate-Restrepo, J.M. Hill, Effect of hydrogen on carbon formation on Ni/YSZ composites exposed to methane, *Appl. Catal. A Gen.* 347 (2008) 106–111.
- [62] Z. Cheng, J.-H. Wang, Y. Choi, L. Yang, M.C. Lin, M. Liu, From Ni-YSZ to sulfur-tolerant anode materials for SOFCs: electrochemical behavior, in situ characterization, modeling, and future perspectives, *Energy Environ. Sci.* 4 (2011) 4380–4409.
- [63] J.-H. Wang, M. Liu, Computational study of sulfur–nickel interactions: a new S–Ni phase diagram, *Electrochem. Commun.* 9 (2007) 2212–2217.
- [64] J. Matienzo, L.I. Yin, S.O. Grim, W.E. Swartz, X-ray photoelectron spectroscopy of nickel compounds, *Inorg. Chem.* 12 (1973) 2762–2769.
- [65] A. Cho, B. Hwang, J.W. Han, Development of Ni-based alloy catalysts to improve the sulfur poisoning resistance of Ni/YSZ anodes in SOFCs, *Catal. Sci. Technol.* 10 (2020) 4544–4552.
- [66] M.U.C. Braga, G.H. Perin, L.H. de Oliveira, P.A. Arroyo, DFT calculations for adsorption of H₂S and other natural gas compounds on (Fe, Co, Ni, Cu and Zn)–Y zeolite clusters, *Microporous Mesoporous Mater.* 331 (2022), 111643.
- [67] C. Jiang, E. Loisel, D.A. Cullen, J.A. Dorman, K.M. Dooley, On the enhanced sulfur and coking tolerance of Ni–Co-rare earth oxide catalysts for the dry reforming of methane, *J. Catal.* 393 (2021) 215–229.
- [68] K.P. Kepp, A quantitative scale of oxophilicity and thiophilicity, *Inorg. Chem.* 55 (2016) 9461–9470.
- [69] J.L. Oliphant, R.W. Fowler, R.B. Pannell, C.H. Bartholomew, Chemisorption of hydrogen sulfide on nickel and ruthenium catalysts: I. Desorption isotherms, *J. Catal.* 51 (1978) 229–242.
- [70] O.I. Malyi, Z. Chen, V.V. Kulish, K. Bai, P. Wu, Density functional theory study of the effects of alloying additions on sulfur adsorption on nickel surfaces, *Appl. Surf. Sci.* 264 (2013) 320–328.
- [71] K. Taira, T. Sugiyama, H. Einaga, K. Nakao, K. Suzuki, Promoting effect of 2000 ppm H₂S on the dry reforming reaction of CH₄ over pure CeO₂, and in situ observation of the behavior of sulfur during the reaction, *J. Catal.* 389 (2020) 611–622.
- [72] J.A. Poston, R.V. Siriwardane, E.P. Fisher, A.L. Miltz, Thermal decomposition of the rare earth sulfates of cerium(III), cerium(IV), lanthanum(III) and samarium(III), *Appl. Surf. Sci.* 214 (2003) 83–102.
- [73] D. Marrocchelli, B. Yildiz, First-principles assessment of H₂S and H₂O reaction mechanisms and the subsequent hydrogen absorption on the CeO₂ (111) surface, *J. Phys. Chem. C* 116 (2012) 2411–2424.